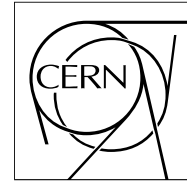


The Compact Muon Solenoid Experiment

CMS Note

Mailing address: CMS CERN, CH-1211 GENEVA 23, Switzerland



Design, Performance, and Calibration of CMS Forward Calorimeter Wedges

G. Baatian, A. Sirunyan

Yerevan Physics Institute, Yerevan, Armenia

I. Emeliantchik, V. Massolov, N. Shumeiko, R. Stefanovich

NCPHEP, Minsk, Belarus

J. Damgov, L. Dimitrov, V. Genchev, S. Piperov, I. Vankov

Institute for Nuclear Research and Nuclear Energy, Bulgarian Academy of Science, Sofia, Bulgaria

L. Litov

Sofia University, Sofia, Bulgaria

G. Bencze, A. Laszlo, A. Pal, G. Vesztergombi, P. Zalan

KFKI-RMKI, Research Institute for Particle and Nuclear Physics, Budapest, Hungary

A. Fenyvesi

ATOMKI, Debrecen, Hungary

H. S. Bawa, S. B. Beri, V. Bhatnager, M. Kaur, A. Kumar, J. M. Kohli, J. B. Singh

Panjab University, Chandigarh, 160 014, India

B. S. Acharya, Sudeshna Banerjee, Sunanda Banerjee, S. R. Chendvankar, S. R. Dugad, S. D. Kalmani,
S. Katta, K. Mazumdar, N. Mondal, P. Nagaraj, M. R. Patil, L. V. Reddy, B. Satyanarayana,
S. Sharma, P. Verma

Tata Institute of Fundamental Research, Mumbai, India

M. Hashemi, M. Mohammadi-Najafabadi, S. Paktinat

Institute for Studies in Theoretical Physics and Mathematics and Sharif University of Technology, Tehran, Iran

K. Babich, I. Golutvin, V. Kalagin, I. Kosarev, V. Ladygin, G. Mescheryakov, P. Moissenz,
A. Petrosyan, E. Rogalev, S. Sergeev, V. Smirnov, A. Vishnevskiy, A. Volodko, A. Zarubin

JINR, Dubna, Russia

V. Gavrilov, Y. Gershtein¹⁾, N. Ilyina, V. Kaftanov, I. Kisselevich, V. Kolossov, A. Krokhotin,

¹⁾ Now at Florida State University, Tallahassee, FL, USA.

S. Kuleshov, D. Litvintsev²⁾, A. Oulyanov, S. Safronov, S. Semenov, V. Stolin

ITEP, Moscow, Russia

A. Gribushin, A. Demianov, O. Kodolova, S. Petrushanko, L. Sarycheva, K. Teplov, I. Vardanyan,
A. Yershov

Moscow State University, Moscow, Russia

V. Abramov, P. Goncharov, A. Kalinin, A. Korablev, A. Khmelnikov, Y. Korneev, A. Krinitsyn,
V. Kryshkin, V. Lukanin, V. Pikalov, A. Ryazanov, V. Talov, L. Turchanovich, A. Volkov

IHEP, Protvino, Russia

T. Camporesi, T. de Visser, E. Vlassov³⁾

CERN, Geneva, Switzerland

S. Aydin, M. N. Bakirci, S. Cerci, I. Dumanoglu, E. Eskut, A. Kayis-Topaksu, S. Koylu, P. Kurt,
A. Kuzucu, G. Onengut, N. Ozdes-Koca, H. Ozkurt, K. Sogut, H. Topakli, M. Vergili, T. Yetkin

¹⁵ *Cukurova University, Adana, Turkey*

K. Cankocak⁴⁾, H. Gamsizkan, C. Ozkan, S. Sekmen, M. Serin-Zeyrek, R. Sever, E. Yazgan,
M. T. Zeyrek

Middle East Technical University, Ankara, Turkey

M. Deliomeroğlu, K. Dindar, E. Gülmez, E. Isiksal⁵⁾, M. Kaya⁶⁾, S. Ozkorucuklu⁷⁾

Bogazici University, Istanbul, Turkey

L. Levchuk, P. Sorokin

KIPT, Kharkov, Ukraine

B. Grinev, V. Lubinsky, V. Senchishin

Single Crystal Institute, Kharkov, Ukraine

E. W. Anderson, J. Hauptman

Iowa State University, Ames, IA, USA

J. Elias, J. Freeman, D. Green, A. Heering⁸⁾, D. Lazic⁹⁾, S. Los, A. Ronzhin, I. Suzuki, R. Vidal,
J. Whitmore

Fermi National Accelerator Laboratory, Batavia, IL, USA

G. Antchev, M. Arcidy, E. Hazen, C. Lawlor, E. Machado, C. Posch, J. Rohlf, L. Sulak, F. Varela,
S. X. Wu

Boston University, Boston, MA, USA

M. Adams, K. Burchesky, W. Qiang

²⁾ Now at FNAL, Batavia, IL, USA.

³⁾ Also with ITEP, Moscow, Russia.

⁴⁾ At Mugla University, Mugla, Turkey.

⁵⁾ At Marmara University, Istanbul, Turkey.

⁶⁾ At Kafkas University, Kars, Turkey.

⁷⁾ At Süleyman Demirel University, Isparta, Turkey.

⁸⁾ Now at Boston University, Boston, MA, USA.

⁹⁾ Now at Boston University, Boston, MA, USA.

University of Illinois at Chicago, Chicago, IL, USA

S. Abdullin, D. Baden, R. Bard, S. Eno, T. Grassi, C. Jarvis, R. Kellogg, S. Kunori, J. Mans¹⁰⁾,
A. Skuja, L. Wang, M. Wetstein

University of Maryland, College Park, MD, USA

S. Ayan, U. Akgun, F. Duru, J. P. Merlo, A. Mestvirishvili, M. Miller, E. Norbeck, J. Olson, Y. Onel,
I. Schmidt

University of Iowa, Iowa City, IA, USA

N. Akchurin¹¹⁾, K. Carrell, K. Gümüş, H. Kim, M. Spezziga, R. Thomas, R. Wigmans

Texas Tech University, Lubbock, TX, USA

M. Baarmand, H. Mermerkaya, I. Vodopianov
Florida Institute of Technology, Melbourne, FL, USA

L. Kramer, S. Linn, P. Markowitz, G. Martinez
Florida International University, Miami, FL, USA

P. Cushman, Y. Ma, B. Sherwood
University of Minnesota, Minneapolis, MN, USA

L. Cremaldi, J. Reidy, D. A. Sanders
University of Mississippi, Oxford, MS, USA

W. Fisher, C. Tully
Princeton University, Princeton, NJ, USA

S. Hagopian, V. Hagopian, K. Johnson
Florida State University, Tallahassee, FL, USA

V. Barnes, A. Laasanen, A. Pompos
Purdue University, West Lafayette, IN, USA

Abstract

We report on the test beam results and calibration methods using high energy electrons, pions and muons with the CMS forward calorimeter (HF). The HF calorimeter covers a large pseudorapidity region ($3 \leq |\eta| \leq 5$), and is essential for large number of physics channels with missing transverse energy. It is also expected to play a prominent role in the measurement of forward tagging jets in weak boson fusion channels. The HF calorimeter is based on steel absorber with embedded fused-silica-core optical fibers where Cherenkov radiation forms the basis of signal generation. Thus, the detector is essentially sensitive only to the electromagnetic shower core and is highly non-compensating ($e/h \approx 5$). This feature is also manifest in narrow and relatively short showers compared to similar calorimeters based on ionization. The choice of fused-silica optical fibers as active material is dictated by its exceptional radiation hardness. The electromagnetic energy resolution is dominated by photoelectron statistics and can be expressed in the customary form as $\frac{a}{\sqrt{E}} \oplus b$. The stochastic term a is 198% and the constant term b is 9%. The hadronic energy resolution is largely determined by the fluctuations in the neutral pion production in showers, and when it is expressed as in the electromagnetic case, $a = 280\%$ and $b = 11\%$.

¹⁰⁾ Now at University of Minnesota, Minneapolis, MN, USA.

¹¹⁾ Corresponding author.

1 Introduction

The forward calorimeters (abbreviated as HF) in the Compact Muon Solenoid (CMS) experiment at the Large Hadron Collider (LHC) cover a large pseudorapidity range, $3 \leq |\eta| \leq 5$, and thus significantly improve jet detection and the missing transverse energy resolution which are essential in top quark production studies, Standard Model Higgs, and all SUSY particle searches [1, 2].

Higgs boson production through weak boson fusion as a potential Higgs discovery channel requires identification of high energy quark jets by the forward calorimeters. This channel is largely characterized by two energetic forward *tagging* jets ($\langle p \rangle \approx 1$ TeV) with a typical transverse momentum of $m_W/2$. The largest suppression against background is achieved by the efficient identification of these tagging jets by the forward calorimeters [3, 4].

We discussed the general features of Cherenkov calorimetry and beam test results from several fused-silica, or quartz for short, calorimeter prototypes in previous papers [5, 6, 7, 8, 9, 10]. The final CMS forward calorimeter design is a culmination of these studies. In this paper, we exclusively concentrate on the test beam measurements of performance of the HF wedges with high energy electrons, pions and muons. In Section 2, a detailed description of HF calorimeters is presented. Section 3 focuses on the experimental setup, followed by Section 4, which summarizes the data analyses and final results. The radioactive source calibration methods are described in Section 5 in detail. The simulation results and comparison with the data are presented in Section 6. Conclusions and the outlook for the HF calorimeters are summarized in the last section (Section 7).

2 Description of HF Calorimeters

The forward calorimeter will experience unprecedented particle fluxes. On average, 760 GeV per proton-proton interaction is deposited into the two forward calorimeters, compared to only 100 GeV for the rest of the detector. Moreover, this energy is not uniformly distributed but has a pronounced maximum at the highest rapidities. At $|\eta| = 5$ and an integrated luminosity of $5 \times 10^5 \text{ pb}^{-1}$ (~ 10 year of LHC operation), the HF will experience ~ 1 GRad. The charged hadron rates will also be extremely high. For the same integrated luminosity, inside the HF absorber at 125 cm from the beam-line, it will range higher than 10^{11} per cm^2 [2]. This hostile environment presents a unique challenge to calorimetry, and the design of the HF calorimeter was first and foremost guided by the necessity to survive in these harsh conditions, preferably for at least a decade. Successful operation critically depends on the radiation hardness of the active material. This was the principal reason why quartz fibers (fused-silica core and polymer hard-clad) were chosen as the active medium.

The signal is generated when charged shower particles above the Cherenkov threshold ($E \geq 190$ keV for electrons) generate Cherenkov light, thereby rendering the calorimeter mostly sensitive to the electromagnetic component of showers [11]. A small fraction of the generated light is captured, $f_{\text{trap}} = \text{NA}/2n_{\text{core}}^2$, in the numerical aperture ($\text{NA} = 0.33 \pm 0.02$), and only half of that ends up on the PMT photocathode. Only light that hits the core-cladding interface at an angle larger than the critical angle (71°) contributes to the calorimeter signal. The half-angle $\theta = 19^\circ$ is determined by the refractive indices of the core (n_{core}) and the cladding (n_{clad}), $\sin \theta = \sqrt{n_{\text{core}}^2 - n_{\text{clad}}^2}$. The fibers measure $600 \pm 10 \mu\text{m}$ in diameter for the fused-silica core, $600 + 5 - 10 \mu\text{m}$ with the polymer hard-clad, and $800 \pm 30 \mu\text{m}$ with the protective acrylate buffer ¹⁾. Over 1000 km of fiber is used in the HF calorimeters and the fibers are cleaved at both ends by a diamond cleaver. We measured the attenuation length of these fibers to be ~ 15 m using high energy electrons at 90-degree to the fibers.

The optical attenuation in these types of fibers scales as $a(\lambda)(D/D_0)^{b(\lambda)}$ where D is the accumulated dose, and it is normalized by a reference dose ($D_0 = 100$ MRad) for convenience. For example, at 450 nm at the accumulated dose of $D = 100$ MRad, the induced attenuation is ~ 1.5 dB/m, which simply equals a . The a and b parameters characterize the radiation hardness of a given fiber. For high OH⁻ (300-500 ppm) HF fibers at 450 nm, $a \approx 1.3$ and $b \approx 0.3$ [12, 13, 14]. An accumulated dose of 1 GRad will result in a loss of optical transmission by a half, which is the worst case for HF after a decade.

The calorimeter consists of a steel absorber structure that is composed of 5 mm thick grooved plates. Fibers are inserted in these grooves. The detector is functionally subdivided into two longitudinal seg-

¹⁾ Manufactured by Polymicro Technologies, LLC, Phoenix, AZ, USA.

ments. Half of the fibers run over the full depth of the absorber ($165 \text{ cm} \approx 10\lambda_I$) while the other half starts at a depth of 22 cm from the front of the detector. These two sets of fibers are read out separately. This arrangement makes it possible to distinguish showers generated by electrons and photons, which deposit a large fraction of their energy in the first 22 cm, from those generated by hadrons, which produce signals in both calorimeter segments. We refer to the long fiber section as L (it measures the total signal), and the short fiber section as S (it measures the energy deposition after 22 cm of steel). The absorber is constructed from 5 mm thick grooved steel plates where the grooves ($0.90 + 0.12 - 0 \text{ mm}$, at the base and by $1.06 + 0.6 - 0 \text{ mm}$ in depth) make a square grid separated by $5.0 \pm 0.1 \text{ mm}$ center-to-center. Long and short fibers alternate in these grooves. The packing fraction by volume (fiber/total) in the first 22 cm is 0.57% and is twice as large beyond that depth.

The forward calorimeter is essentially a cylindrical steel structure with an outer radius of 130.0 cm. The front face of the calorimeter is located at 11.15 m from the interaction point. A cylindrical hole for the beam pipe is at radius 12.5 cm from the center of the beam line. Thus, the effective sensitive radial interval is 117.5 cm. This structure is azimuthally subdivided into 20-degree modular wedges for practical reasons. Thirty-six such wedges (18 on either side of the interaction point) make up the HF calorimeters. We exposed 6 of these wedges in the beam and report the results in this paper. A cross section view of the HF is shown in Figure 1. The fibers run parallel to the beamline, and are bundled to form 0.175×0.175 in $\Delta\eta \times \Delta\phi$ towers (Figure 2). The detector is housed in a hermetic radiation shielding which consists of layers of 40 cm thick steel, 40 cm of concrete, and 5 cm of polyethylene. A large plug structure in the back of the detector provides additional shielding.

Bundled fibers are held in ferrules which illuminate one end of the air-core light guides that penetrate through 42.5 cm of shielding matrix (steel, lead, and polyethylene). This shielding is necessary to protect the photomultipliers and the electronics housed in the readout boxes. The air-core light guide consists of a hollow tube inlined with highly reflective custom-made sheets. These metal-coated reflectors are designed to be very efficient ($> 90\%$) in the visible spectrum at the relevant angles for our application (~ 70 degrees from normal). Light typically makes five bounces before reaching the photocathode and nearly half the light is lost in this transport. Each light guide is coupled to a standard bialkalinic, 8-stage photomultiplier tube with a borosilicate glass window²⁾. A readout box (RBX) houses 24 PMTs and services half of a wedge (10^0).

The entire calorimeter system with its shielding components is mounted on a rigid table which supports more than 240 tonnes with less than 1 mm deflection. The absorber alone weighs 108 tonnes. The table is also designed for vertical separation of the detector into two sections to clear the beam pipe at installation and removal. It is possible to align the forward calorimeters within $\pm 1 \text{ mm}$ with respect to the rest of the CMS experiment.

3 Experimental Setup

The measurements described in this paper were performed at the H2 test beam line of the Super Proton Synchrotron at CERN. The HF wedges were individually placed on a remotely controlled table that could move horizontally and vertically with respect to the beam with better than 1 mm precision. The positioning of the detector at an angle on the vertical plane with respect to the beam line was also remotely controlled and varied from 0° to 6° to mimic the particle path in the CMS experiment.

The beam particle rates were typically several thousand per spill. The spill lasted 2.6 s and were repeated at every 14.4 s. The purity of the beam depended on energy, in particular high energy electron beams were contaminated with pions and muons.

The beam line was equipped with trigger and tracking detectors and Figure 3 schematically shows the detector positions. The trigger condition was based on signals from several scintillating counters located upstream of the HF wedge: SC-1 ($14 \text{ cm} \times 14 \text{ cm}$), SC-2 ($4 \text{ cm} \times 4 \text{ cm}$), SC-3 ($2 \text{ cm} \times 2 \text{ cm}$), SC-4 ($14 \text{ cm} \times 14 \text{ cm}$), SC-5 ($5 \text{ cm} \times 8 \text{ cm}$), and SC-6 ($5 \text{ cm} \times 8 \text{ cm}$). The first four counters were positioned between 12.8 to 13.8 m from the front face of the HF wedge. A $16 \text{ cm} \times 16 \text{ cm}$ scintillator veto counter (VC) with a 5 cm diameter hole in the center was positioned midway between SC-5 and SC-6, positioned at 1.63 m and 1.60 m, respectively. A large scintillation counter behind one meter of iron tagged muons with high efficiency (MC).

²⁾ (R7525) Manufactured by Hamamatsu Photonics, Japan.

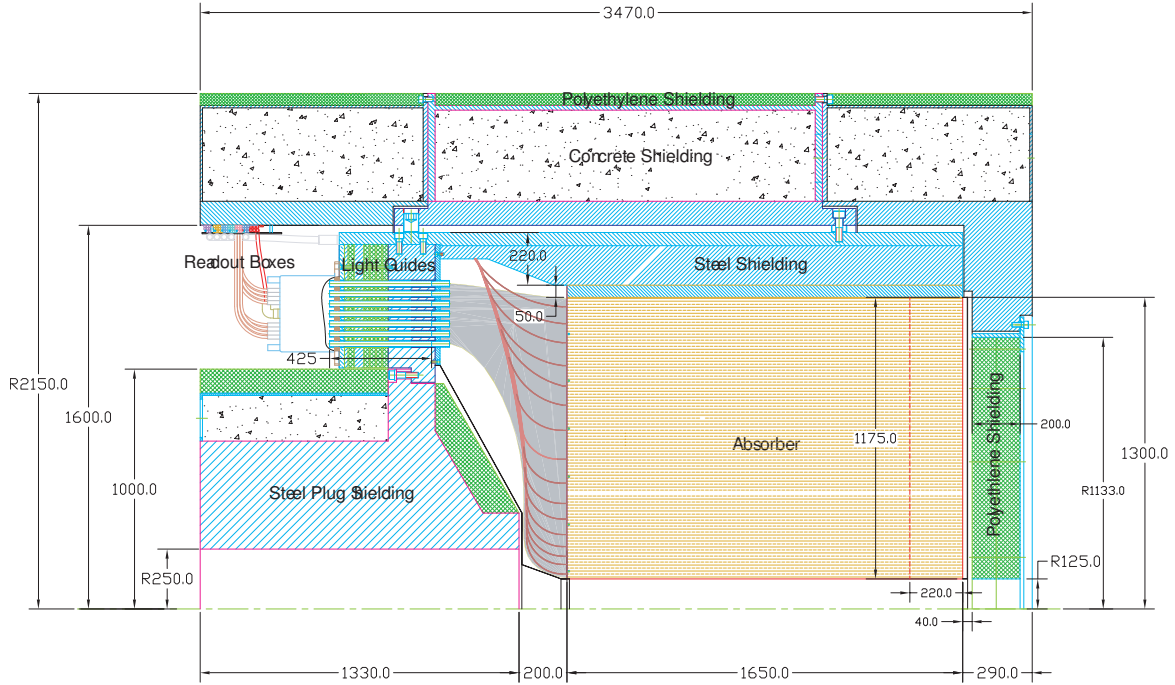


Figure 1: The cross section view of the HF calorimeter shows that the sensitive area extends from 125 to 1300 mm in the radial direction. The absorber in the beam direction measures 1650 mm. Bundled fibers (shaded area) are routed from the back of the calorimeter to air-core light guides which penetrate through a steel-lead-polyethylene shielding matrix. Light is detected by PMTs housed in the readout boxes. Stainless steel radioactive source tubes (red lines) are installed for each tower and are accessible from outside the detector for source calibration. The intersection point is at 11.15 meters from the front of the calorimeter to the right. All dimensions are in mm.

Table 1: The tower sizes, number of fibers, bundle sizes and the percentage of photocathode area utilized are listed below for each tower. The air-core light guides are tapered to better match the photocathode area for towers 1, 2 and 3.

Ring No	(r_{in}, r_{out}) [mm]	$\Delta\eta$	$\Delta\phi$ [degree]	N_{fib}	A_{bundle} [mm ²]	$\frac{A_{bundle}}{A_{photocathode}}$
1	(1162-1300)	0.111	10	594	551	1.14
2	(975-1162)	0.175	10	696	652	1.33
3	(818-975)	0.175	10	491	469	0.96
4	(686-818)	0.175	10	346	324	0.66
5	(576-686)	0.175	10	242	231	0.47
6	(483-576)	0.175	10	171	167	0.34
7	(406-483)	0.175	10	120	120	0.25
8	(340-406)	0.175	10	85	88	0.18
9	(286-340)	0.175	10	59	63	0.13
10	(240-286)	0.175	10	41	46	0.94
11	(201-240)	0.175	10	30	35	0.71
12	(169-201)	0.175	20	42	52	0.11
13	(125-169)	0.300	20	45	50	0.10

Five multiwire proportional chambers (indicated as WC-A through WC-E) were located at 1.0, 2.2, 12.7, 14.7, and 15.7 m from the HF wedge. These chambers were used to reconstruct each incoming particle's track. The space resolution was better than 0.5 mm with over 90% track reconstruction efficiency.

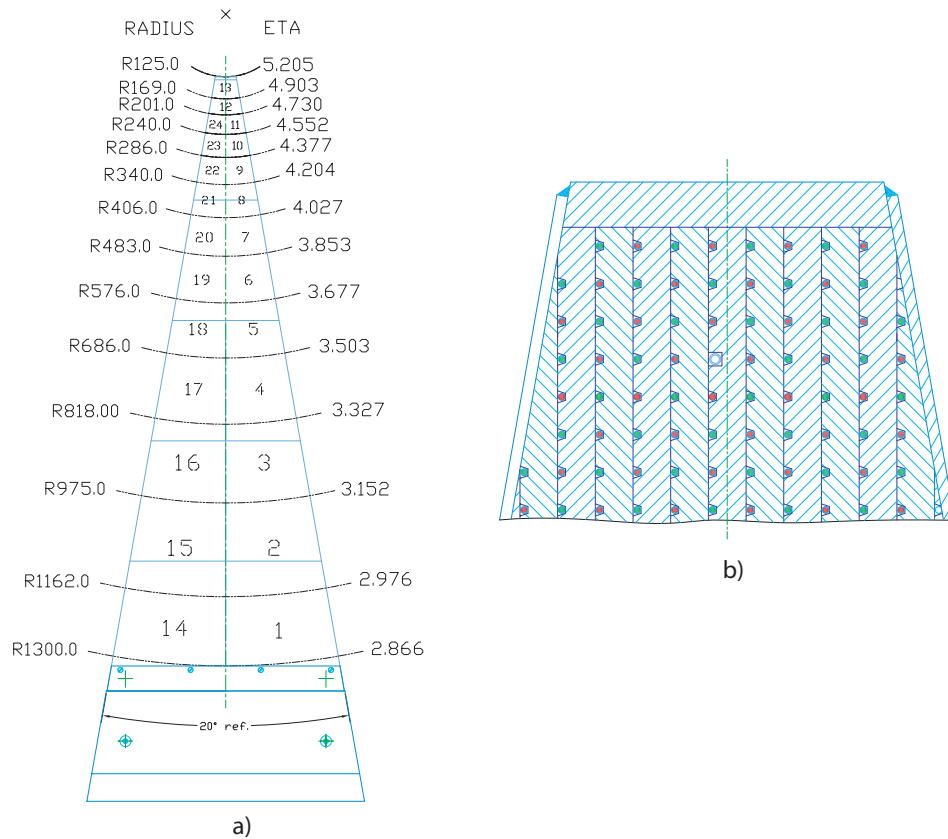


Figure 2: The transverse segmentation (Table 1) is 0.175×0.175 in $\Delta\eta \times \Delta\phi$ with the exception of two towers (12 and 13) at the tip of the wedge near the beam pipe (a). An expanded view of tower 13 shows the radioactive source tube in the center of the tower. Long and short fibers alternate and are separated by 5 mm (b).

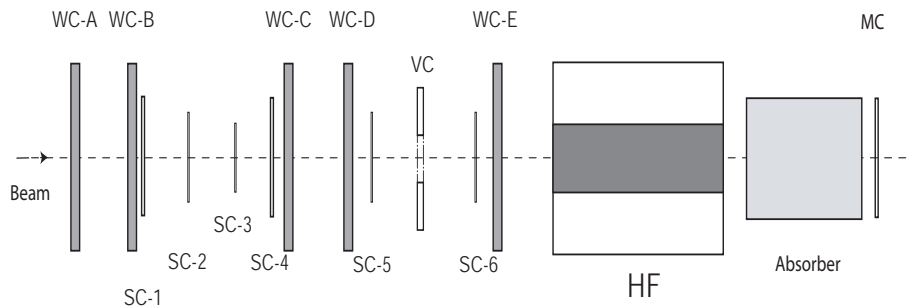


Figure 3: The schematic view of the beam line at the CERN H2 beam line for the HF calorimeter tests is depicted above. A single HF wedge, mounted on a specially designed table, could be remotely moved in horizontal and vertical directions, as well as tilted in the vertical plane up to 6 degrees with respect to the beam direction.

4 Data Analyses and Results

4.1 Energy Calibration

The energy calibration of the HF wedges was accomplished by using 100 GeV electrons for both the long (L) and short (S) fiber sections. Six wedges were scanned in 2.5 cm steps horizontally and vertically. In order not to be sensitive to transverse leakage from the sides of the wedge, we demanded that the particle impact point be at least 2 cm inside the edges during off-line analyses. For all electrons hitting tower i , we calculate A_{ij} as the average signal in tower j . For each L section tower i , we required the full wedge signal to electrons to be equal to 100 GeV of the beam energy.

$$A_{ij}w_j = 100 \text{ GeV} \quad (1)$$

where w_j is the unknown calibration coefficient for tower j . In each wedge, there are 24 L and 24 S channels ($i = 1, \dots, 24$). Solving these 24 linear equations, we first determined the calibration constants for all L type towers. The calibration of the S towers relied on the same procedure where the total S signal was set to 30 GeV. This was done because the PMT gains for the S section were known compared to the PMT gains for the L section with precision and this was also verified with Monte Carlo. Typically, the average PMT gain set for Wedge 2-13 was 14.9 fC/GeV for L , and 9.8 fC/GeV for S . For Wedge 2-6, the PMT gains on average were somewhat lower where the average L gain was 12.3 fC/GeV and 7.2 fC/GeV for S .

4.2 Linearity and e/π Ratio

The wedges were tested at 30, 50, 100, and 150 GeV with electrons. The linearity of electromagnetic response was within $\pm 2\%$ for long fibers in this energy range (Figure 4). The electromagnetic response from short fibers is nonlinear due to effectively 22 cm deep steel absorber in front of them. At 30 GeV, only 20% of energy is detected by the short fibers. This percentage increases to 35% at 150 GeV.

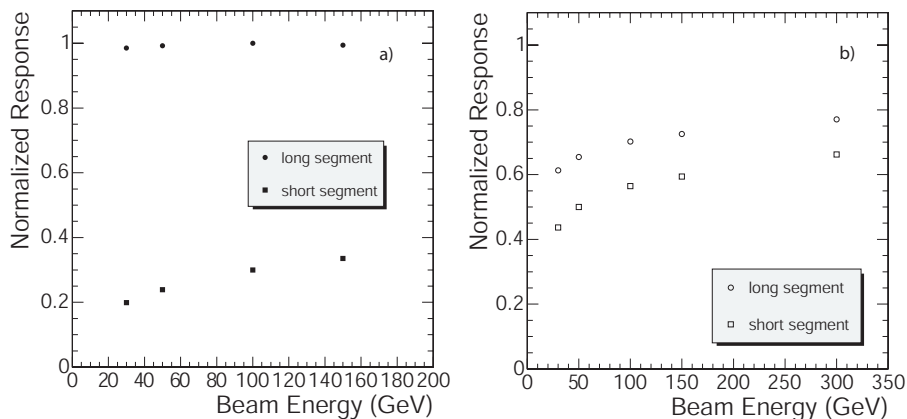


Figure 4: The normalized response to electrons for long fibers (a) is within $\pm 2\%$ in the tested range of 30 to 150 GeV. The short segment response is nonlinear due to effectively uninstrumented 22-cm thick steel section in front. The pion response (b) in the range of 30 to 300 GeV is normalized to electron, and shows characteristic nonlinearity, especially at lower energies, for both sections.

Figure 5 shows the total ($L + S$) response versus beam energy for electrons and pions with no special weighting. The e/π response varies between 1.14 to 1.01 from 30 to 150 GeV. The detector was designed such that the e/π response would be as flat as possible as a function of particle energy. This specific feature, although less than perfect at very low energies, follows from the particular choice of fiber lengths for the L and S sections with the ultimate intention that the jet energy response be as linear as possible.

The variation in response from six different towers in two wedges to electrons and pions is shown in Figure 6. When normalized to the electron response at 100 GeV (Figure 6.a and 6.b), the L response does not vary more than $\pm 1.4\%$. The variation in S section remains well within $\pm 2.5\%$. These do not exceed $\pm 4\%$ in the case of pions although we did not make transverse leakage corrections. The overall

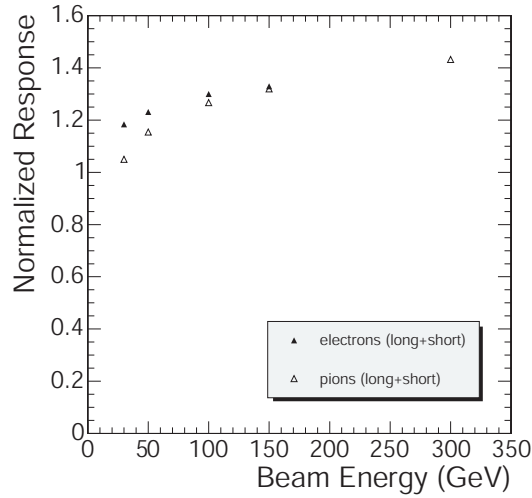


Figure 5: The $L + S$ response of the detector for electrons and pions are shown as a function of beam energy. The e/π ratio varies from 1.14 to 1.01 in the tested energy range, and is essentially flat at high energies.

effect of these differences from one part of the detector to another does not affect the stochastic term in the energy resolution appreciably and the constant term varies by no more than 2%.

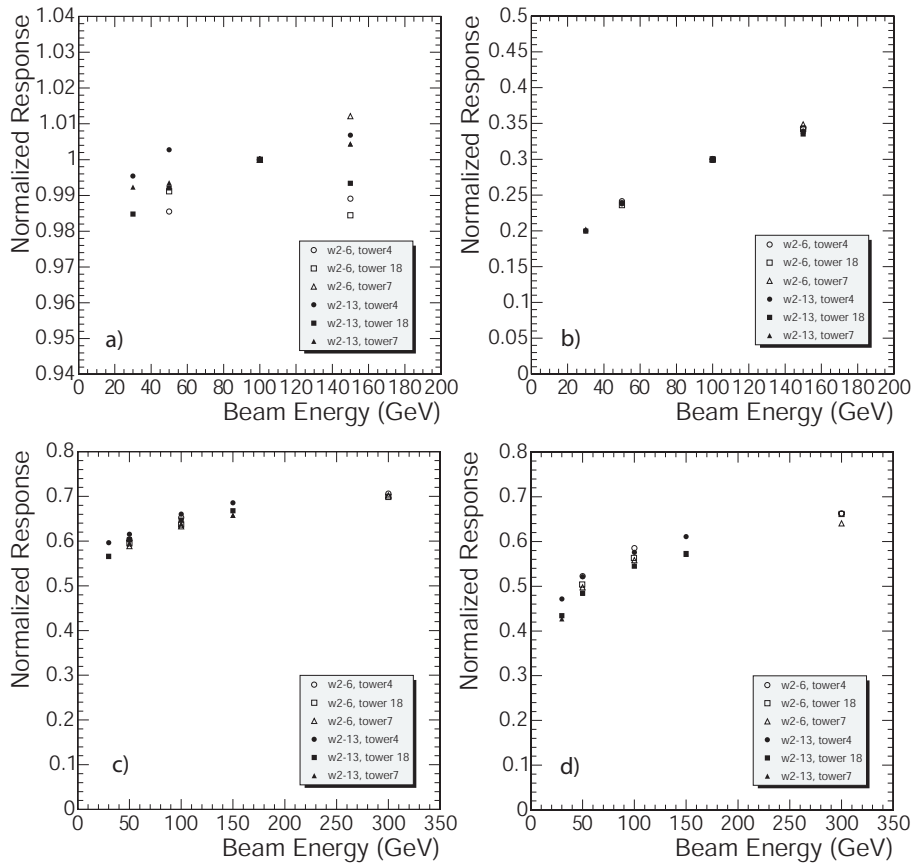


Figure 6: The electron responses from six different towers from 30 to 150 GeV are normalized at 100 GeV for both the L (a), and the S (b) sections. The variations are well within $\pm 2.5\%$. The variations in pion response from 30 to 300 GeV for both the L (c), and the S (d) sections of the calorimeter are well within $\pm 4\%$.

4.3 Energy Resolution

Figure 7 shows the L , S , and summed $L + S$ response functions for 50 GeV and 150 GeV electrons. The detector is calibrated (see Section 4.1) such that the summed electron signal from all the long fiber towers equals the beam energy. The mean signal from the short section for 50 GeV electrons is about 24% of the beam energy, 11.95 GeV. The combined signal with equal weights is 61.56 GeV. Similarly, the long fiber section gives 149.1 GeV for 150 GeV electrons, and the short section results in 35% of beam energy, 50.35 GeV. Note that as the beam energy increases the detector response function tends to a Gaussian distribution.

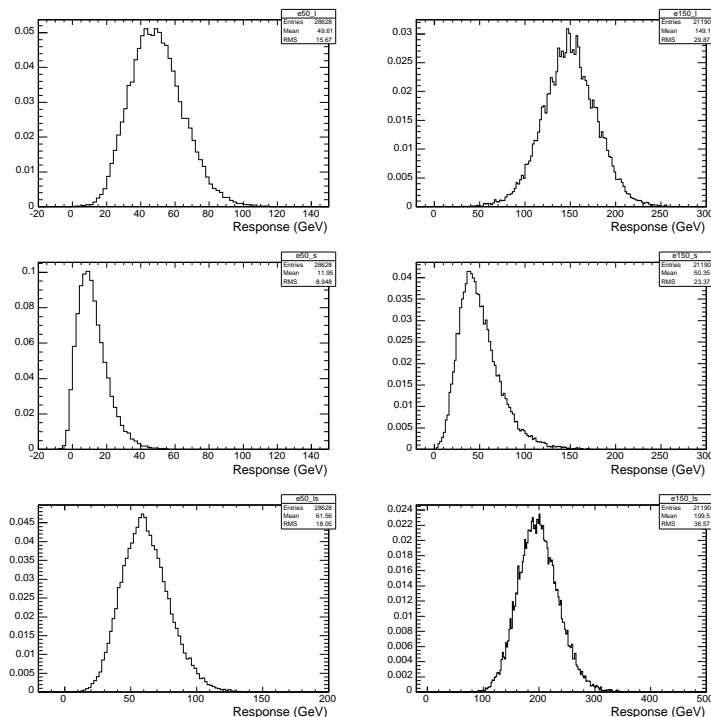


Figure 7: The response functions for 50 (left) and 150 (right) GeV electrons from the long (top), short (middle), and combined $L + S$ (bottom) signals are shown above. All distributions are normalized such that their integrals equal unity.

The electromagnetic resolution of the HF calorimeter is dominated by photoelectron statistics (Figure 8). At 50 GeV, $\sim 29\%$ out of $\sim 32\%$ of the electromagnetic energy resolution is due to the stochastic term. The photoelectron yield is 0.24 pe/GeV. The constant term ($\sim 10\%$) is dominated by structural non-uniformities. Since the fiber-to-fiber distance represents a significant fraction of the Molière radius, the calorimeter response depends on the impact point of the particles. It is smallest for impact points midway between two fibers, and increases as the impact point approaches a fiber. The addition of S to L signals improves the overall electromagnetic resolution somewhat. The stochastic term decreases by 10.5% due to increased photoelectron yield.

The sampling frequency contribution to a is considerably smaller compared to that of the photoelectron statistics and it amounts to 47% for L and 33% for $L + S$ for electromagnetic showers.

Figure 9 displays the same experimental data as in Figure 8.a for the L and $L + S$ signals where the square of electromagnetic energy resolution is plotted against $1/E$. We calculate the expected $L + S$ resolution (shown in black squares) from the energy resolution obtained from the L section alone but the stochastic term is scaled by $\sqrt{L/(L+S)}$, and the same 10.7% constant term is added point by point in quadrature to give us the expected $L + S$ resolution. Close similarity between the expected and the measured energy resolutions for the same constant term of 10.7% suggest that attributing significance to the differences in the fitted constant terms (L vs $L + S$) is not warranted.

The hadronic π^0 energy resolution is largely determined by π^0 fluctuations in showers (Figure 8.b). At low energies, 30 GeV and less, the photoelectron statistics also contribute. It is practical to parametrize the

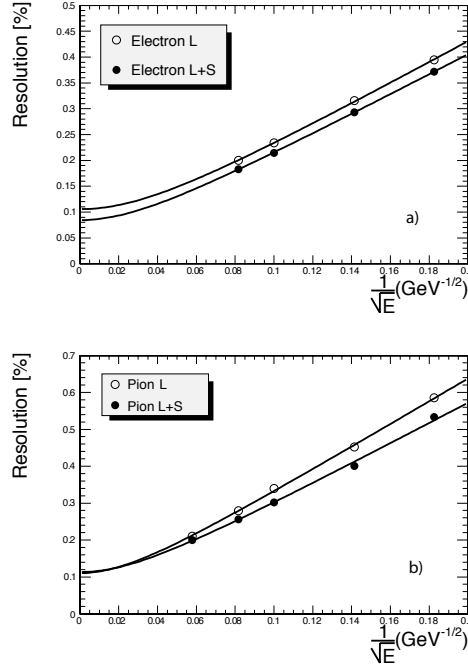


Figure 8: The electromagnetic energy resolution (a) is dominated by the photoelectron statistics and thus is parametrized as $a/\sqrt{E} \oplus b$. The energy resolution due only to the long (L) fibers results in 208% for the stochastic term a and 11% for the constant term b . The addition of S fibers improves the energy resolution to 198% and 9% for stochastic and constant terms, respectively (Table 8). The hadronic energy resolution (b), on the other hand, is largely determined by the fluctuations in the neutral pion content of the showers. At lower energies, photoelectron statistics also contribute. When parametrized as $\frac{a}{\sqrt{E}} \oplus b$, $a = 314\%$ and $b = 11\%$ due to L fibers. For ($L + S$), the values are $a = 280\%$ and $b = 11\%$ (Table 9).

hadronic energy resolutions in the same way as the electromagnetic energy resolution is expressed, *i.e.* a stochastic term a which scales with $(1/\sqrt{E})$ and a constant term b . In order to properly account for the effects of non-compensation, we analyzed deviations from $E^{-1/2}$ scaling (E in GeV) by expressing the hadronic energy resolution as:

$$\frac{\sigma}{E} = \frac{a'}{\sqrt{E}} \oplus b' \left[\frac{E}{0.7} \right]^{-0.28} \oplus c'. \quad (2)$$

However, because of the strong correlation between the different terms and the relatively small energy range and limited number of the data points, it is difficult to minimize this expression reliably. Nevertheless, we attempt to analyze these fit values because of their inherent and relevant physical meaning for this detector. The coefficient b' is equal to 0 for a compensating ($e/h = 1$), and $b' = 1$ for highly non-compensating ($e/h = \infty$) detector ($b' = 1 - h/e$). In Table 2, we list a set of values for a' , b' , and c' where some of the parameters are fixed in the minimization process, and they are indicated with \pm . The stochastic term, a' , improves when S signal is added to L , although with large errors, without much change in b' . If the 30 GeV data point is left out of the fit to avoid systematics associated with low photoelectron yield at this energy, $a' = 2.20 \pm 0.06$ and $b' = 0.83 \pm 0.03$. We expect $b' \approx 0.8$ which results

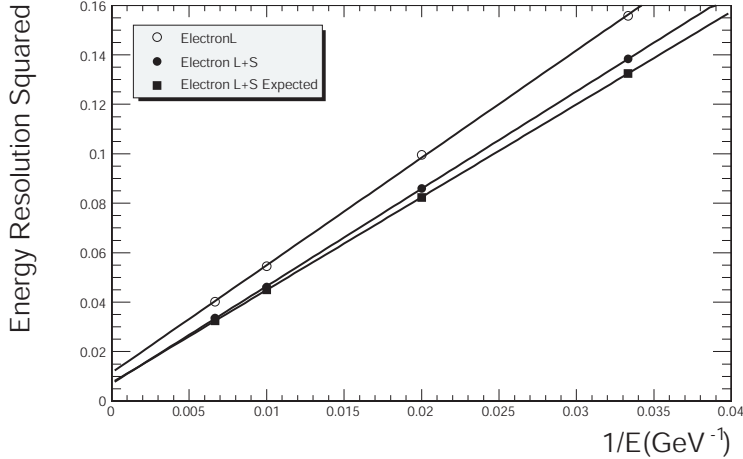


Figure 9: The electromagnetic energy resolution squared for the measured L and $L+S$ signals are plotted against $1/E$. The expected energy resolution points for the $L+S$ are indicated in black squares for the same assumed constant term as in the case of L , 10.7%.

in $e/h \approx 5$. If we impose $b' = 0.83 \pm 0$ on L only signal, the stochastic term turns out to be 2.71 ± 0.04 . There is a further constraint on a' values for L and $L+S$ assuming exact $1/\sqrt{E}$ scaling. As is discussed in Section 4.7, we find $\langle \alpha_\pi \rangle = (L-S)/(L+S) \approx 0.1$. Thus, we expect the stochastic term for $L+S$ to be improved by a factor of $1.81^{-1/2}$ compared to a' for L only ($2.71 \times 1/\sqrt{1.81} = 2.01$ vs 2.20). Although agreement is not perfect, but within errors, it is sufficient to illustrate the salient features with limited data.

The combined $L+S$ signal improves the hadronic energy resolution in the low energy range, where sampling fluctuations and photoelectron statistics (factors affecting the value of α in Section 4.7) contribute significantly to this resolution.

All energy resolutions are calculated using Wedge 2-13 and tower 18. The track of the incoming particle is determined by using WC-A, WC-B, WC-D, and WC-E and the track quality is controlled by $\chi^2/\text{ndf} < 10$ in either plane.

Table 2: The electromagnetic and hadronic energy resolutions for single particles are summarized below. Note that the values are quoted in percent, while E is in GeV. Dagger indicates 30 GeV data point is left out of the fit.

Parametrization	Fiber Sections	a (a')	b (b')	c'
$(\frac{\sigma}{E})_{EM} = \frac{a}{\sqrt{E}} \oplus b$	L	208.4 ± 1.3	10.7 ± 0.4	-
	$L+S$	197.9 ± 0.6	8.6 ± 0.2	-
$(\frac{\sigma}{E})_{HAD} = \frac{a}{\sqrt{E}} \oplus b$	L	313.5 ± 2.9	11.2 ± 0.9	-
	$L+S$	279.9 ± 4.7	11.4 ± 1.4	-
$(\frac{\sigma}{E})_{HAD} = \frac{a'}{\sqrt{E}} \oplus b' [\frac{E}{0.7}]^{-0.28} \oplus c'$	L	290 ± 7	68 ± 6	1 ± 0
	$L+S$	256 ± 15	66 ± 12	1 ± 0
	$L+S^\dagger$	220 ± 6	83 ± 3	1 ± 0
	L	271 ± 4	83 ± 0	1 ± 0
	L^\dagger	264 ± 3	83 ± 0	1 ± 0
	L^\dagger	278 ± 3	75 ± 0	1 ± 0

4.4 Angular Dependence

As noted earlier, the angle between the fiber axis and the particle trajectories from the interaction point in the CMS experiment will range from 0.5 to 6 degrees. In order to evaluate the significance of this angle on the detector performance, an angle scan in the vertical plane was carried out. Figure 11 displays

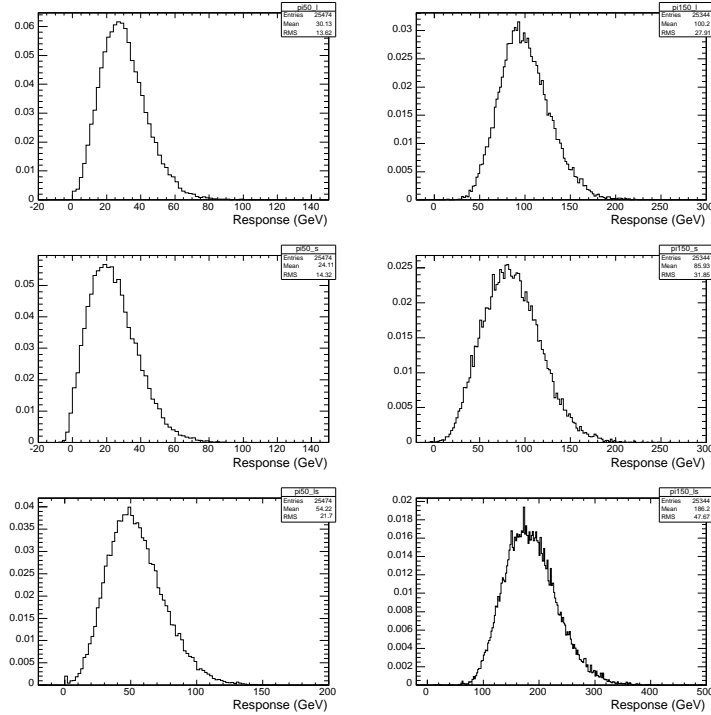


Figure 10: The response functions for 50 (left) and 150 (right) GeV pions from the long (top), short (middle) and the combined $L + S$ (bottom) signals are shown above. All distributions are normalized such that their integrals equal unity.

the results for the L fiber section for 100 GeV electrons. The data sample comes from a detector area of 1.6 mm in the horizontal and 60 mm in the vertical direction centered along a column of fibers. As the impact angle increases from 0 to 4 degrees (Figure 11.a-c), the response oscillation with a 10 mm period as a function of particle impact point is removed. The level of variation is as large as $\pm 30\%$ at 0 degree. At 2 degrees, it is down to $\pm 8\%$ and is essentially removed at 4 degrees. The comparison of the response functions between 0 and 4 degrees indicates that at smaller angles, the response function is effectively a sum of many different response functions (corresponding to different impact points) where the long tail in Figure 11.d originates from the shower core near the fiber. As the angle increases, the sampling frequency too increases which results in a more uniform signal.

In order evaluate the effect of these oscillations on the constant term of the electromagnetic energy resolution, we analyze the magnitude of these oscillations at 2 degrees –the same angle at which all energy measurements were performed. These variations for L , S , and the summed $L + S$ signals for 100 GeV electrons in an area of 30 mm wide in horizontal and 10 mm high in vertical are depicted in Figure 12. The L section displays $\pm 6\%$ while the S shows large $\pm 17\%$ oscillations. We expect 11.1 GeV oscillations for the $L + S$ case, which amounts to 8.5% (11.1/130), in good agreement with what was measured (see Table 2).

4.5 Transverse Shower Shapes

The transverse shower profile has a very steep radial dependence. The Cherenkov fiber calorimeters are predominantly sensitive to the electromagnetic shower core which is, on average, cylindrically symmetric around the shower axis. In the case of electrons, beyond 5 cm from the shower axis, only $\sim 2\%$ of the energy remains. Beyond 1.0 cm, fiber-to-fiber distance, all but about 15% of the total energy is absorbed. In the case of hadrons showers, the transverse shower profile is less steep compared to that of the electrons: beyond 1 cm 30%, and beyond 5 cm 10% of the energy remains unaccounted for.

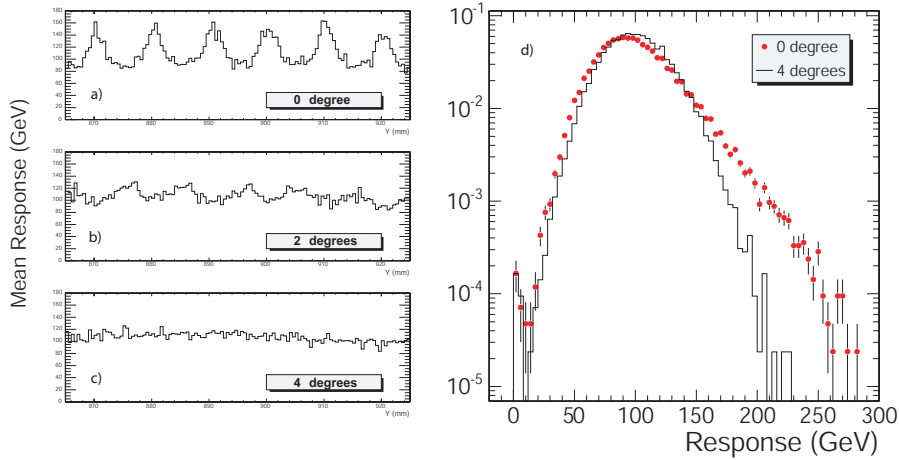


Figure 11: The response variation as a function of particle impact point is illustrated for an area 1.6 mm wide horizontal and 60 mm high vertical area for 100 GeV electrons. The higher response comes from the at the location of fibers. As the angle between the particle path and the fiber axis increases (a-c), the detector responses become uniform.

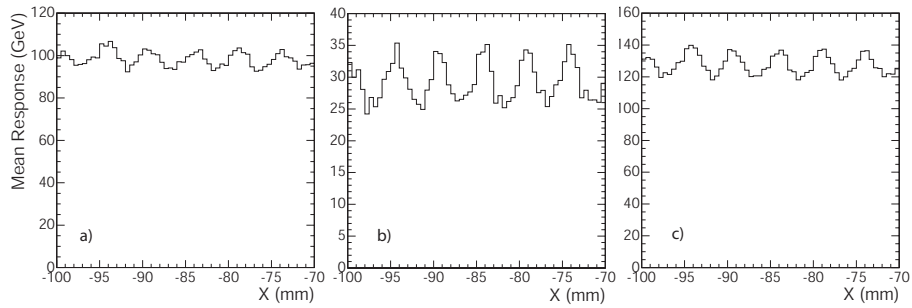


Figure 12: The response variations (in GeV) as a function of particle impact position for 100 GeV electrons are measured for L (a), S (a), and the combined $L + S$ (c) signals for a 30 mm by 10 mm strip. The detector is positioned at 2 degrees on the vertical plane with respect to the beam direction.

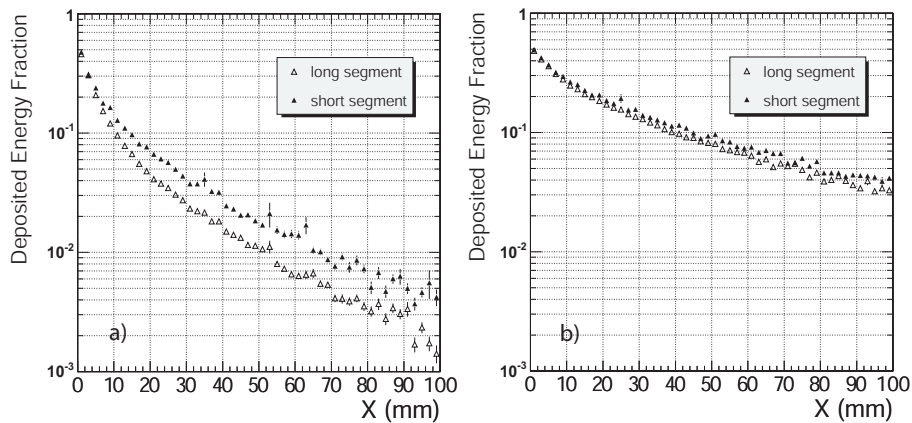


Figure 13: The measured transverse shower shapes for electrons (a) and pions (b) indicate that the energy is concentrated near the shower axis. Beyond 5 cm from the shower axis, only $\sim 2\%$ of the electromagnetic and $\sim 10\%$ of hadronic energy remain.

4.6 Muon Response

We investigated the response of the HF calorimeter to high energy muons for several practical reasons. For example, we wanted to quantify the most probable energy equivalent signal if a muon hit a PMT

and/or densely packed fiber bundles behind the absorber. The muon particle selection required a good signal from a large muon counter (MC) located behind one meter of iron block and a good track definition from the upstream wire chambers. It was required that 3 out of 5 wire chambers give good hit (x and y) information and that the chi-square for the fitted track is less than 20. We found that when a muon impacts a PMT, it generates on average 120 ± 38 GeV (or 30 photoelectrons) equivalent signal (Figure 14.a). If we assume $N_0 \approx 100 \text{ cm}^{-1}$ for R7525 type PMTs, we conclude that the average glass thickness l that a muon traverses is about 0.6 cm from $N_{p.e.} \approx lN_0 \langle \sin^2 \theta_c \rangle$. Figure 15 shows that the signal generated when a muon impacts the fiber bundle ranges between 50 to more than 100 GeV equivalent signal. In practice, these types of events are easily identified by requiring correlations between L and S signals: for example, a large S signal without an accompanying L signal, or *vice versa*, may be attributed to such a muon event.

The zero-suppressed energy response distribution for 150 GeV muons is shown in Figure 14.b, where a clear single photoelectron peak is visible at 4 GeV.

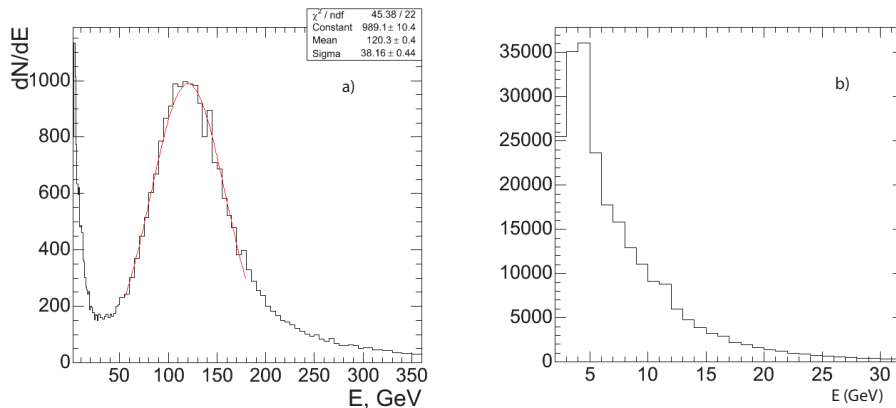


Figure 14: High energy muons impacting the PMT glass generate spuriously large energies (a). The zero-suppressed energy loss distribution clearly shows the single p.e. peak at 4 GeV, as expected.

High energy muons deposit energy as they traverse the calorimeter by radiative process and the total deposit approximately scales with the length of fibers in the detector. Figure 16 shows the response functions for the L and S sections up to 200 GeV. The mean values, however, are indicated for the untruncated spectra where the mean energy loss is 1.26 GeV for the L and 1.16 GeV for the S sections.

4.7 Particle Identification

The response differences between the L and S fibers for electrons and pions are shown in Figure 4. Although the HF calorimeter is optimized for jets, some particle identification is possible by making selective use of the information inherent in these signals. On average, the difference in response between the L and the S sections for electrons is ~ 0.7 , whereas for pions, $\langle L - S \rangle$ ranges between ~ 0.08 to ~ 0.15 in the tested energy range.

The α parameter represents the asymmetry in energy sharing between the L and S fibers and is defined as

$$\alpha = \frac{L - S}{L + S}. \quad (3)$$

If α is near zero, it indicates that the long and short fiber sections register equivalent amount of energy. If $\alpha > 0$, the energy is deposited near the front of the detector and thus, it is likely that the particle is an electron or a photon. If, on the other hand, $\alpha < 0$, deeply penetrating shower has fluctuated and generated a large signal in the short fibers. At all energies, the electrons generally give $\alpha \geq 0.5$ whereas the pions generate relatively wide distributions and tend to peak at $\alpha \approx 0$. As the particle energy increases, both distributions become narrower without significant shifts in the peak positions, thus allowing a better separation efficiency between electrons and pions.

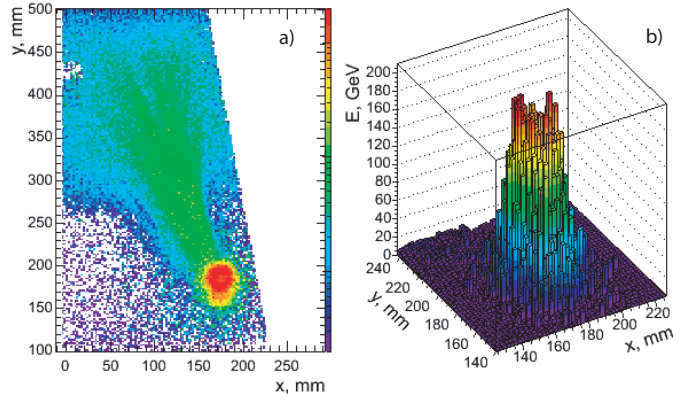


Figure 15: The muon response from a region around a PMT is shown with a $2 \times 2 \text{ mm}^2$ resolution (a). If 150 GeV muons impact the PMT glass after traversing the HF absorber, they generate signals that are equivalent to 120 GeV (b). The L fiber section of tower 15 from Wedge 2-6 is shown as an example.

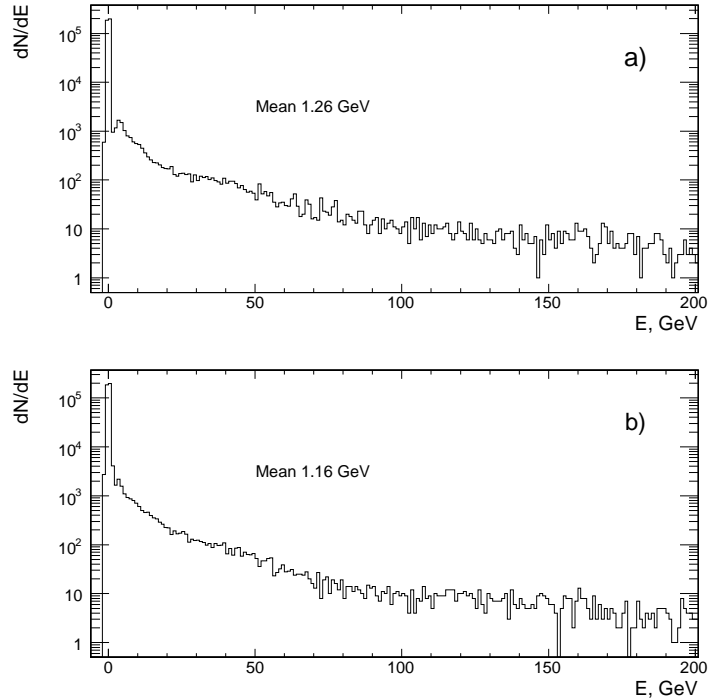


Figure 16: Tower 16 mean signals from the L (a) and the S (b) sections are different by $\sim 8\%$ which nearly scales as with the fiber lengths for L (165 cm) and S (143 cm).

The α parameter makes use of the available information in the longitudinal direction. We also reconstruct another parameter, β , to take advantage of the differences in the radial shower shapes of electrons and pions to further augment particle identification.

$$\beta = \frac{(L + S)_{max}}{\sum_i (L + S)_i} \quad (4)$$

where $(L + S)_{max}$ is maximum energy in a given tower for a single particle and the summation runs over all neighboring towers, including the one with the highest energy. Figure 17 shows α against β for 100 GeV electrons (black) and pions (red) impacting randomly towers 3 and 16. To reduce the effect of the shower leakage, the impact points were required to be within $\Delta\phi = 5^\circ$ from the median of the wedge, that is only a half of either tower was considered. Each event corresponds to a single point in the plot. There is a clear qualitative separation between the electrons and pions. In order to quantify this particle identification, a cut of the form $a\alpha + \beta > A$ is applied. Figure 18 displays the effectiveness of this treatment.

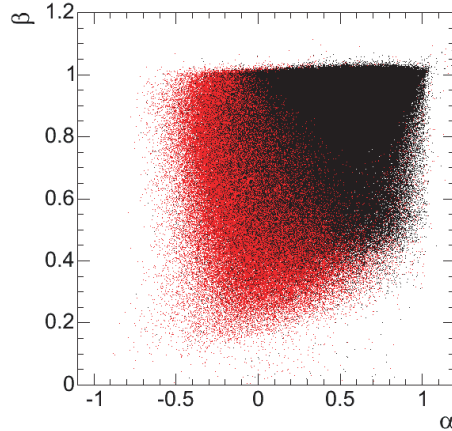


Figure 17: Although HF is not designed for particle identification, we explore its limits by taking advantage of the pseudo-longitudinal segmentation and radial shower sharing between towers. Here, α vs β parameters are plotted for 100 GeV electrons (black) and pions (red).

The fraction of electrons surviving $a\alpha + \beta > A$ is referred to as the electron identification efficiency, while the fraction of surviving pions is called the pion misidentification probability. In Figure 18.a, the electron identification efficiency is plotted against the pion misidentification probability for different choices of a . A cut on the α parameter alone effectively corresponds to large a values ($a = \infty$). This cut is good for moderate pion rejection when the high electron efficiency should be preserved. The β parameter is less effective in this case because it removes electrons close to tower boundaries whose energies are shared by two or more towers. For a stronger pion rejection, however, the β parameter needs to be included in the cut to achieve an optimal performance. For $a = 0.5$, pion misidentification is lowest for essentially all electron identification efficiencies.

Figure 18.b compares the $a = 0.5$ curve with two curves obtained using independent cuts on α and β . These two curves correspond to the fixed cuts on β ($\beta > 0.90$ and $\beta > 0.95$), and the α threshold is varied to yield different values of electron efficiency. Clearly, the independent cuts do not improve the pion rejection compared to the $0.5\alpha + \beta > A$ cut which shows a balanced performance in a large range of electron efficiencies.

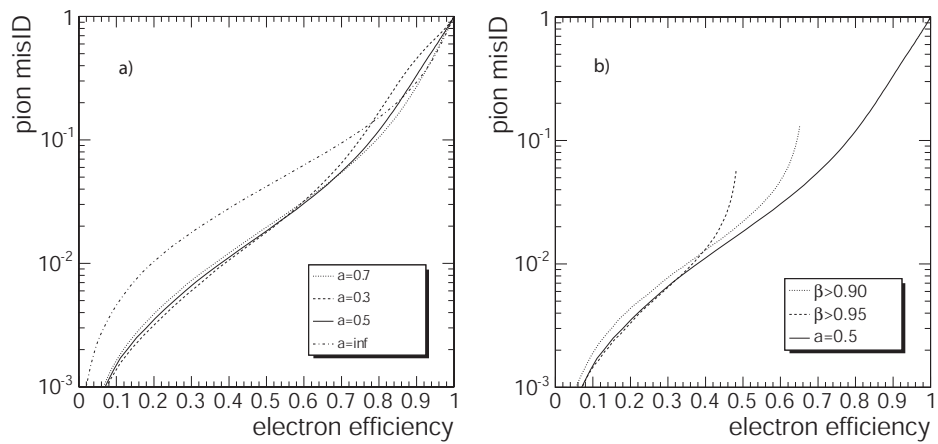


Figure 18: Pion misidentification probability *vs* electron identification efficiency for $a * \alpha + \beta > A$ cut (a) and for independent cuts on α and β (b). Different points on any given curve correspond to different values of A for fixed values of a parameter (a) and to different cuts on α for fixed cuts on β (b).

4.8 Response Uniformity

We measured the uniformity of the detector response over its surface with 100 GeV electrons and pions in order to evaluate the impact of local non-uniformities on energy resolution. A telescope of wire chambers in front of the detector allowed us to determine the impact point of the particles. For each event, the signals from all channels were summed to reconstruct the total response of the detector in GeV. The response of the detector as a function of the impact point on the surface is shown in Figure 19 for L type towers for 100 GeV electrons.

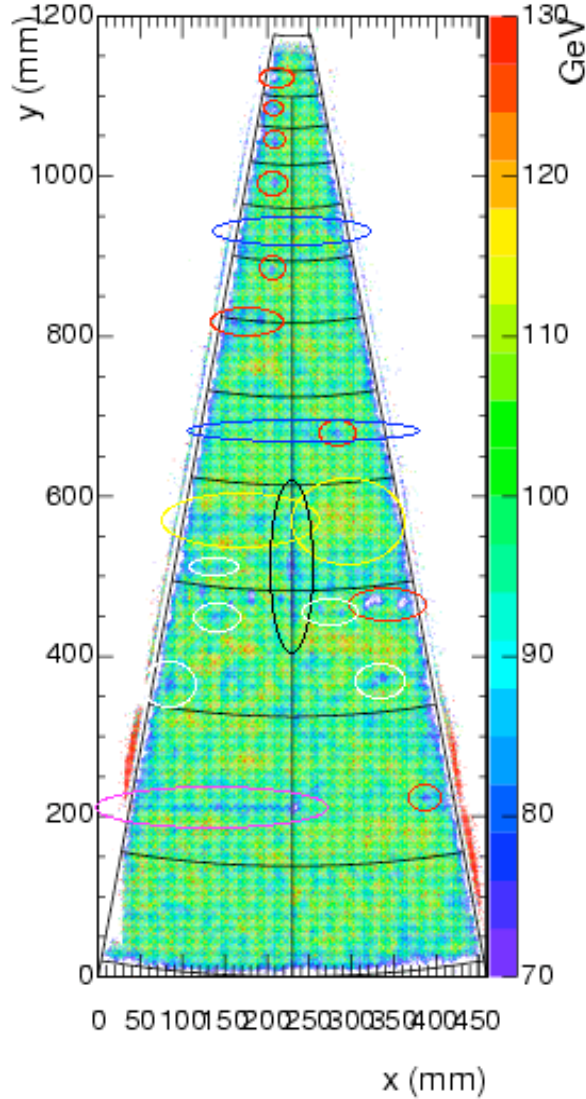


Figure 19: The response of Wedge 2-13 (L signals only) to 100 GeV electrons is measured by moving the calorimeter in a 2.5 cm square grid. Circled areas correspond to different sources of non-uniformity as described in the text.

Based on Figure 19, we classify the sources of non-uniformity into six types:

1. Small dead regions limited to one single fiber (red contour in Figure 19). These often correspond to the location of a source tube, as shown in Figure 20. We also observe that the region where the response is suppressed is limited to a small area around one fiber position. In rare cases, this may extend to a group of apparently broken and/or damaged fibers, as is the case for Tower 16 (Figure 21).

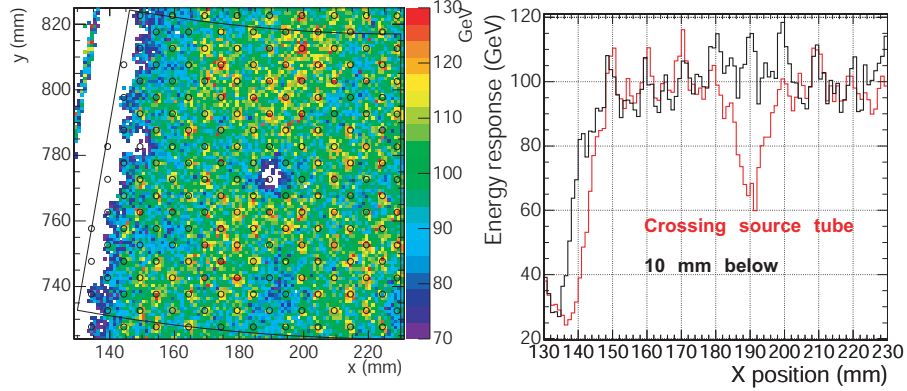


Figure 20: The response distribution for Tower 6 in Wedge 2-14 clearly shows the locations of long (L) fibers as indicated by black open circles as well as the location of a single source tube (in position of an L fiber in this case) where there is $\sim 15\%$ response loss.

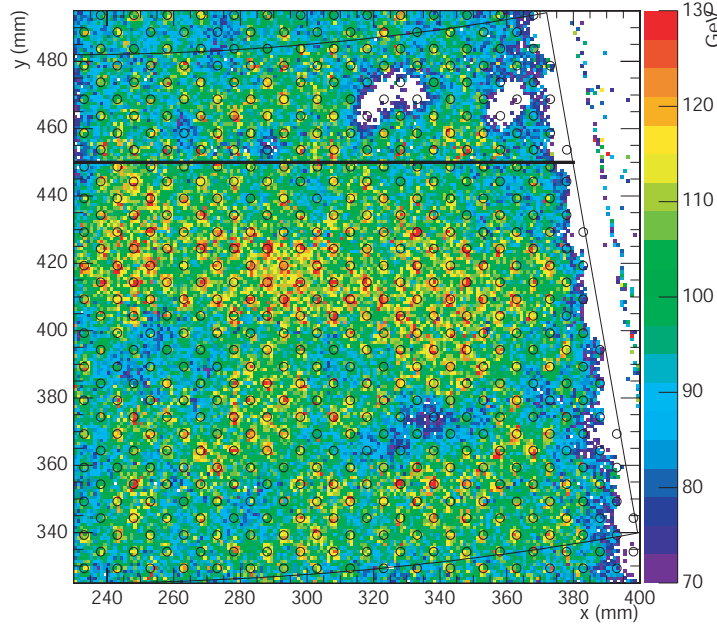


Figure 21: The response of Tower 16 in Wedge 2-13 shows the location of fibers and particularly the low response corresponding to groups of presumably broken and/or damaged fibers.

2. Irregularity in the grid structure of fibers (blue contour in Figure 19) is shown in Figure 22 for Tower 21. This is due to the construction of the wedge where the edges of physical blocks do not correspond to tower borders. At regions where blocks are joined, the distance between rows of fibers are different from the rest of the wedge (5 mm). Therefore, this area may be more or less responsive depending on the local fiber density.
3. Low response regions limited to one single fiber are indicated by white contours in Figure 19. This is different from (1) in that the fiber is not completely dead but perhaps badly cleaved, cracked, or damaged. It is not always possible to distinguish this case from (1).
4. Lines of low electromagnetic response and high hadron response (black contour in Figure 19) are attributed to cracks in the wedge structure, where an electron travels through the crack between physical blocks before interacting deeper in the calorimeter.

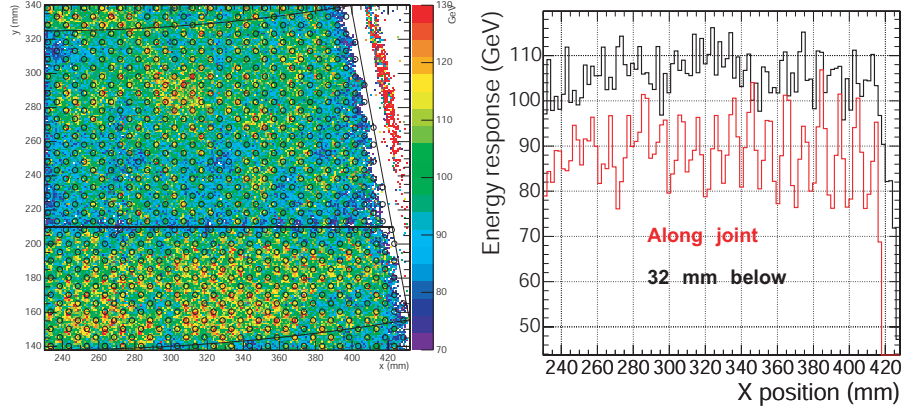


Figure 22: The response of Tower 15 in Wedge 2-14 is down by 10% along the physical joint between the absorber blocks that form this tower (see Figure 2).

5. Lines of low electromagnetic response and uniform hadron response (violet contour in Figure 19). This is either a physical block edge where we have not been able to discern any irregularity in the fiber grid (type 2) or a crack where the hadron response is too small to confirm the presence of the crack (type 4).
6. Relatively large areas of higher or lower response of the wedge, not related to any of the above defects (yellow contour Figure 19). This is the most serious source of non-uniformity because it affects large areas and is comparable to the expected jet sizes. The sources of these non-uniformities range from poor ferrule construction to the regions of poor reflection in the air-core light guides.

The relevant question is how these non-uniformities affect the energy resolution. In order to quantify the effects of forementioned non-uniformities, we first define uniformity in a way that allows us to measure it and evaluate its contribution to the resolution of the detector. If we divided the wedge into small enough cells (*e.g.* fiber-to-fiber distance scale), we could assume that the responses within these small cells are uniform. Thus, we then define the response of each cell as the average response to electrons impacting that cell.

In Figure 23, we observe that the non-uniformity contribution to the energy resolution decreases with the increasing cell size because the response is less sensitive to small-scale non-uniformities. The average resolution of the cells is denoted by σ_c . The contribution of non-uniformity is expressed by σ_U and it is zero when the detector is perfectly uniform. We conclude that for all sources of non-uniformities described above, the degradation in resolution is no more than 1 to 2%, for 100 GeV electrons.

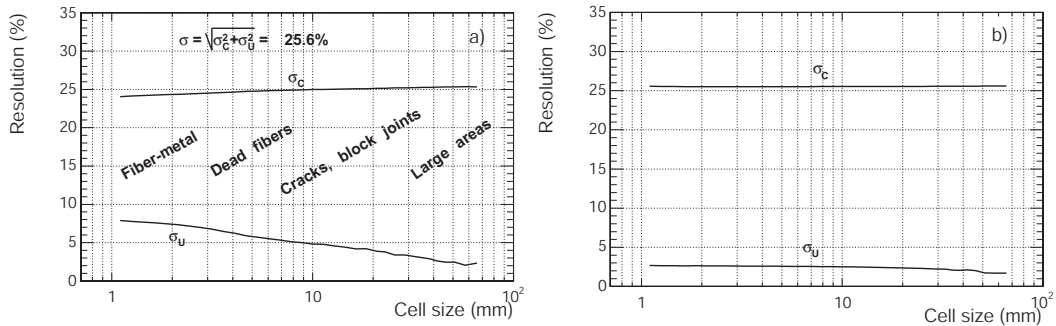


Figure 23: The values of σ_U and σ_c as a function of the cell size show that the non-uniformities contribute to the electromagnetic energy resolution at the level of $\sim 2\%$ at 100 GeV, *e.g.* Wedge 2-13, (a). The same evaluation is shown for 150 GeV pions in (b).

The same analysis is shown in Figure 23.b for 150 GeV pions, where the larger shower size smears out the small scale non-uniformities. Therefore no significant increase in σ_U takes place for cell sizes of order

of 1 to 10 mm.

4.9 HF Pulse Shape

One of the unique features of the HF response is its speed. Figure 24 shows the deconvoluted pulse shapes for electrons and pions for the long and short fiber sections. More than 90% of the charge is within a single LHC bunch crossing (25 ns). The hadronic showers on average indeed develop deeper in the detector compared to the electromagnetic ones. The deeper shower signals do reach the PMTs earlier because of the fact that the generated light travels shorter (fiber) distance. The difference between the electromagnetic ($t_{max}^{EM} \approx 15$ cm) and the hadronic ($t_{max}^{HAD} \approx 32$ cm) shower maxima is about 17 cm, which corresponds to ~ 1 ns time difference between the arrivals of electron and pion signals to the PMTs, in good qualitative agreement with Figure 24.

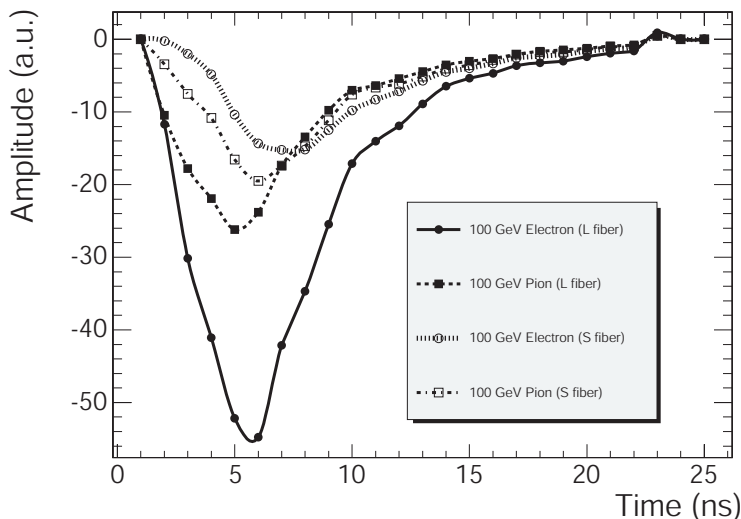


Figure 24: The peak position of pulses from 100 GeV electrons is ~ 1 ns later compared to that of pions at the same energy. The average distance between electromagnetic and hadronic shower maxima is ~ 17 cm.

The signal traces displayed in Figure 24 come from Wedge 2-6, Tower 2 (see Figure 2.a). The total integrated charge for the *S* section for 100 GeV electrons is 30% that of *L*. For 100 GeV pions, for the *L* section, we expect 65% of what is observed for the same energy electrons for the same fiber section (see Figure 4.b). Due to sizable transverse shower leakage, we register $\sim 48\%$. For the *S* section, we see $\sim 40\%$ instead of the expected 54% due to transverse leakage as well.

5 Calibration and Monitoring

There are three separate but complementary calibration and monitoring systems in HF: radioactive sources, LEDs and lasers. These systems fulfill different functions. While we use the radioactive sources for calibration, the LED and lasers are typically useful for PMT gain measurements, signal timing as well as front-end electronics debugging and monitoring.

5.1 ^{60}Co Signal and Calibration

Gamma rays from ^{60}Co ($t_{1/2} = 5.27$ years) create Compton electrons, and the ones above Cherenkov threshold generate photons in the fibers. The resulting signal, mostly consisting of single photoelectrons, is used to calibrate the calorimeter. A set of devices capable of inserting a long thin wire, of length up to ~ 11 m, containing a point-like radioactive *seed* into a succession of hundreds of thin conduits (source tubes) embedded in the calorimeters has been developed for this purpose.

The PMT signals are digitized by QIEs. QIE is an acronym for the functions of the ASIC, Q (charge), I (integration) and E (encode). A large dynamic range is accomplished through a multi-range technique.

The input current is simultaneously integrated on all four ranges, and comparators are used to select the lowest range that is not at full scale. The selected voltage representing the integrated charge is then put through an on-chip Flash ADC. The outputs are a 5-bit mantissa representing the voltage and a two-bit code indicating the range. Operations are time multiplexed and pipelined to allow signals to settle and to make the reset interval the same as the integration interval. Clocking takes place at 40 MHz and the latency is 100 ns as the pipeline is four clock cycles deep. For a given charge deposition over a clock interval, no more than one capacitor in the set will have its voltage within specified limits. The Flash ADC is piecewise linear. It is built with 15 bins weighted 1, 7 bins weighted 2, 4 bins weighted 3, 3 bins weighted 4, and 3 bins weighted 5. The priority encoded address of the capacitor makes up the exponent bits. The voltage on the capacitor is the mantissa and the address of the capacitor is the exponent.

In a special histogramming mode specifically designed for use with radioactive sources, a special module builds the histogram at the sampling rate. Once 4×2^{12} samples are accumulated, the histogram is readout by the data acquisition system. Therefore, one histogram corresponds to 6.55 ms of source data. In a typical source calibration run, the source is driven at 10 cm/s, which corresponds to over 2500 such histograms while the source is inside the absorber.

Figures 25.a and 25.c show the response of HF to a 5 mCi ^{60}Co source as a function of the source position. The source enters the absorber at 445 cm.

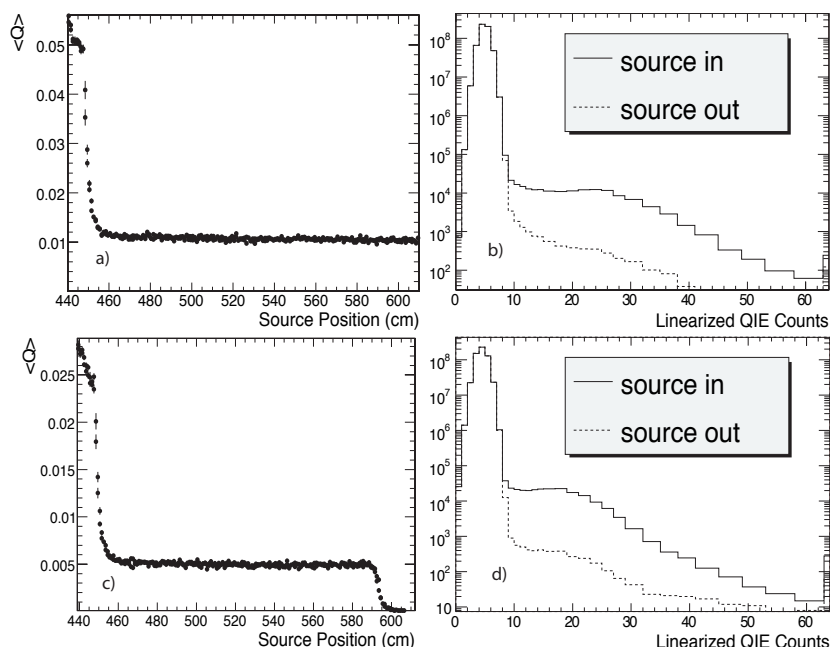


Figure 25: The left plots shows the response of a detector tower as a function of the source position: L signal in (a) and S in (c). The mean response in linearized QIE counts is plotted against the source position inside the source tube. The histograms on the right clearly display the difference between the observed source signal and the background.

The radioactive source excites a small region around its location; 90% of the signal originates from a region with a radius of 3 cm, with fibers near the source contributing to the signal the most.

We summarize three different approaches to using radioactive sources in calibration in our specific case.

1. The shift in the mean value of the source histogram with respect to the pedestal (no-source) events is stable at a level of 10^{-3} QIE counts. The calibration precision that we are able to attain using this approach is $\sim 10\%$. We calculate the mean charge per event for a given tower as follows:

$$\langle Q \rangle = \frac{f}{N} \sum_{i=1}^{32} n_i q_i \quad (5)$$

where f is the 40 MHz sampling frequency, N is the total number of events in the histogram ($N = \sum_{i=1}^{32} n_i$), and n_i is the number of events in the i th bin. q_i represents the charge for the i th bin. There are 32 bins ($i = 1, \dots, 32$) in the histogram and they are weighted nonlinearly. The mean value for the background (b) (no source) is subtracted from the mean value calculated for the signal (s) for each tower j :

$$\langle Q_j \rangle = \langle Q_j^{(s)} \rangle - \langle Q_j^{(b)} \rangle. \quad (6)$$

The energy deposited in an infinitely large tower per unit time (E) by the source is equal to the average charge per unit time $\langle Q_j \rangle$ divided by the geometric correction factor R_j and multiplied by the calibration coefficient C_j . The geometric correction factors are calculated using Monte Carlo techniques to account both for the energy leakage out of j th tower and the relative position of the source tube with respect to the fibers –the source tubes are either located in place of a L or S type fiber. Since the tower at the thinner side of the wedge (high rapidity) are considerably smaller compared to the size required to contain the source activity, this correction factor is necessary. The R value is 0.4 for the smallest of the towers, and it exceeds 0.9 for the larger ones. Thus,

$$E = \frac{C_j}{R_j} \langle Q_j \rangle. \quad (7)$$

The energy deposited depends on the activity of the source and the energy absorbed by the detector, *i.e.*, $E = a\epsilon$, where a is the activity of the source in mCi and the ϵ is the energy registered for a mCi source by an infinitely large tower. We calculate ϵ by considering all beam data from the tested wedges (5 wedges and 48 towers each) such that the calibration coefficients C_j^{source} and C_j^{beam} are the same, separately for L and S type towers:

$$\frac{1}{5} \sum_{k=1}^5 \left(\sum_{j=1}^{24} \frac{C_j^{\text{source}}}{C_j^{\text{beam}}} \right) = 1. \quad (8)$$

We find $\epsilon = 2.38 \times 10^4$. Table 3 shows the mean values and the *rms* values for $\frac{C_j^{\text{source}}}{C_j^{\text{beam}}}$ for the tested wedges. In general, L type PMTs have higher gains by 50% or more compared to the S type towers, and therefore the *rms* values are smaller. In general, the precision of this method is limited by the PMT gains and the pedestal stability. Small fluctuations in pedestal stability affect this precision strongly since there are several orders of magnitude more pedestal events than source events. Figure 26 shows the $\frac{C_j^{\text{source}}}{C_j^{\text{beam}}}$ ratios for L and S type towers and the distribution of these values which indicate the precision achievable by this technique.

Table 3: The averaged $\frac{C_j^{\text{source}}}{C_j^{\text{beam}}}$ and the *rms* values for five different wedges show that the level of calibration procedure attainable by the use of mean charge technique is limited to 5 to 10% for the L type, and 10 to 20% for the S type towers.

Wedge No.	L Mean	L rms	S Mean	S rms
2-02	1.001	0.092	0.986	0.175
2-04	0.996	0.063	0.930	0.153
2-06	0.985	0.059	1.064	0.138
2-13	0.997	0.045	1.025	0.077
2-14	1.003	0.110	1.014	0.094

- Integrating selected *bins* in the source histogram that are least affected by the pedestal fluctuations and other instrumental effect results in improvement of calibration precision.

$$\langle Q \rangle = \frac{f}{N} \sum_{i=10}^{30} n_i q_i \quad (9)$$

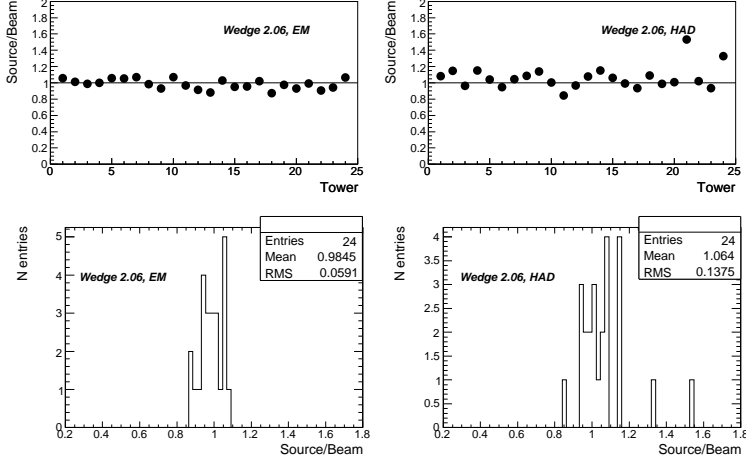


Figure 26: The individual $\frac{C_j^{\text{source}}}{C_j^{\text{beam}}}$ ratios for wedge 2-06 are plotted separately for L and S type towers using the mean charge method. The rms values are 0.059 and 0.138 for the L and S type towers, respectively.

If the integration range is limited to $10 \leq i \leq 30$, the calibration precision is 5% for the L and about 7% for the S type towers. Table 4 summarizes the results. The limitation of this approach is that single photoelectron signal can be shared in two or more QIE time slices. Thus, the charge calculated with the chosen bin interval is only a fraction of the total. These fluctuations greatly contribute to the rms values in Table 4 and Figure 27.

Table 4: The averaged $\frac{C_j^{\text{source}}}{C_j^{\text{beam}}}$ and the rms values for five different wedges show that the level of calibration procedure attainable by the use of the fixed interval technique is limited to $\sim 5\%$ for the L type, and $\sim 7\%$ for the S type towers.

Wedge No.	L Mean	L rms	S Mean	S rms
2-02	1.020	0.051	0.947	0.091
2-04	1.030	0.056	0.909	0.087
2-06	1.016	0.047	1.001	0.072
2-13	1.036	0.045	1.006	0.063
2-14	1.004	0.067	1.039	0.065

- Another approach to source calibration is to subtract the background histogram from the source histogram and extrapolate the resulting histogram with a horizontal line from a chosen bin interval (12 to 16, in this case) to zero (see Figure 28). The resulting histogram is negative for the low counts because there are more pedestal counts in the background histogram than in the signal histogram since the number of entries in both histograms is the same. This extrapolation is arbitrary because the signal contribution under the pedestal peak is unknown.

Figure 29 displays the attainable precision using the extrapolation prescription. Table 5 summarizes the results for five tested wedges. As noted earlier, we rely on the calculated geometric correction factors R_j for each tower, and these factors are most significant for the smallest towers. These values are computed for an ideal wedge and do not take into account wedge to wedge variations. If, for example, the smallest two towers are not included in the rms calculations, there is $\sim 1\%$ gain in calibration precision.

5.1.1 Source Driver System

The source wire is a 22 gauge type 304 stainless steel hardened hypodermic tube with $OD = 0.711$ mm and $ID = 0.406$ mm. The tip is melted shut and then formed into a smooth bullet nose. To reduce

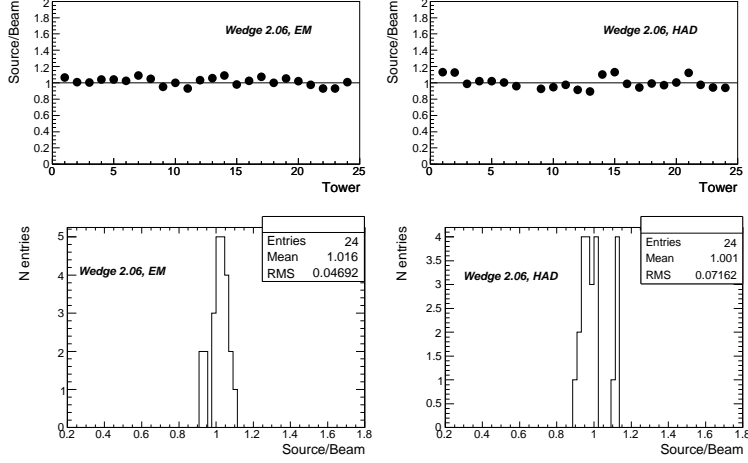


Figure 27: The individual $\frac{C_j^{\text{source}}}{C_j^{\text{beam}}}$ ratios for wedge 2-06 are plotted separately for L and S type towers using the fixed bin interval method. The rms values are 0.047 and 0.072 for the L and S type towers, respectively.

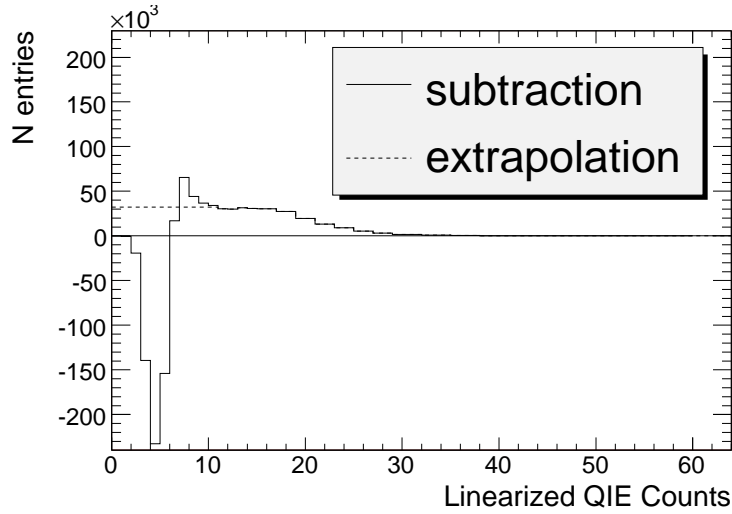


Figure 28: The solid line is the result of the subtraction of the background histogram from the source histogram. The dashed horizontal line from 12 to 0 is an extrapolation employed by this calibration method.

Table 5: The averaged $\frac{C_j^{\text{source}}}{C_j^{\text{beam}}}$ and the rms values for five different wedges show that the level of calibration procedure attainable by the use of the extrapolation prescription is limited to $\sim 5\%$ for the L type and $\sim 6\%$ for the S type towers.

Wedge No.	L Mean	L rms	S Mean	S rms
2-02	0.982	0.047	0.980	0.066
2-04	1.005	0.051	0.954	0.071
2-06	0.987	0.045	1.044	0.053
2-13	0.992	0.043	1.031	0.039
2-14	1.041	0.070	0.993	0.045

friction, the wire is chemically plated. A seed, which is a wire of length ~ 1 mm and OD 0.254 mm,

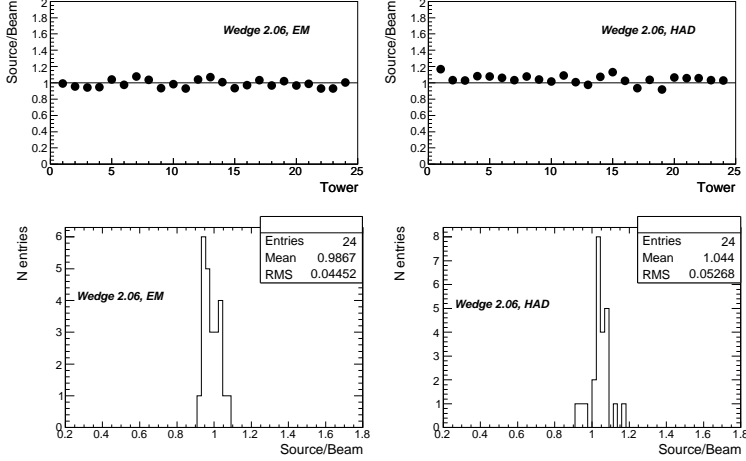


Figure 29: The individual $\frac{C_j^{\text{source}}}{C_j^{\text{beam}}}$ ratios for Wedge 2-06 are plotted separately for L and S type towers using the extrapolation prescription described above. The *rms* values are 0.045 and 0.053 for the L and S type towers, respectively.

nickel plated (the primary encapsulation) after activation in the neutron flux of a reactor, is inserted into the opposite end of the 22 gauge hypodermic wire, pushed into place at the bullet-tip, and held there by a fine steel piano wire of OD = 0.330 mm. The back end of the hypodermic tube is then crimped to the piano wire.

The source wire is attached to a Lexan polycarbonate reel, with a storage groove 0.99 mm wide, 12.7 mm deep, and 25.4 cm in diameter. The reel is belt-driven by a small DC reversible electric motor. The reel faces a low-friction slide sheet on an aluminum plate and turns on a central axle. There is a down-ramped exit groove in the plate leading from a point of tangency at the groove to the edge of the plate, thence into a stainless steel tube which is inside of a lead garage (pig) approximately 10 cm long and 6 cm in diameter. The steel tube is free to slide inside the pig.

At the opposite end of the pig, an S-shaped flexible Nylon tube, 3.18 mm OD, leads from the sliding steel tube to an indexer nozzle (which can be moved-in either a spiral or a straight-line pattern) along a succession of locations in a tightly-packed linear array of 3.18 mm OD plastic tubes, which lead to various locations (towers) within the calorimeter. The air-motor source driver indexers are straight-line and serve of order one hundred tubes. An electric-motor source driver indexer serves up to 396 source tubes. The air-motor driver indexing uses a lead-screw with a pitch of one tube per revolution. The electric-motor driver indexing uses a Geneva drive mechanism which advances the output shaft by 10 degrees once per revolution of the input shaft, followed by a timing-belt gear reduction to the indexer arm.

A button attached to the sliding steel tube actuates a micro-switch when the source wire is extended with sufficient force. This senses that the wire has either encountered the closed end of a source tube or encountered large friction. The end of tube force is adjustable with a small coil compression spring, and typically must be limited to around 1.1 kg-weight to prevent buckling of the source wire in the reel storage groove.

The reel has a spiral groove with limit stops that strike a finger on a sliding arm to stop the reel from overextending and, upon garaging, to stop the wire with the tip in the center of the garage pig. The sliding arm engages micro-switches to turn off the reel motor. In the DC motor drivers, a diode in parallel with each micro-switch permits the reel to drive away from the limit. In the air-motor drivers, a simple TTL logic circuit has the same functionality.

To extend the wire the outer wall of the groove pushes the wire at a downward angle through the exit groove in the aluminum plate. To retract the wire, the inner wall of the groove pulls the wire. The resulting downward wrap of the wire is relieved (by briefly reversing the reel motion) at least twice per revolution to prevent friction-locking as the wire is being stored. Four spring fingers poke through the aluminum plate into the storage groove to tuck the source wire into place as it is being stored. To help

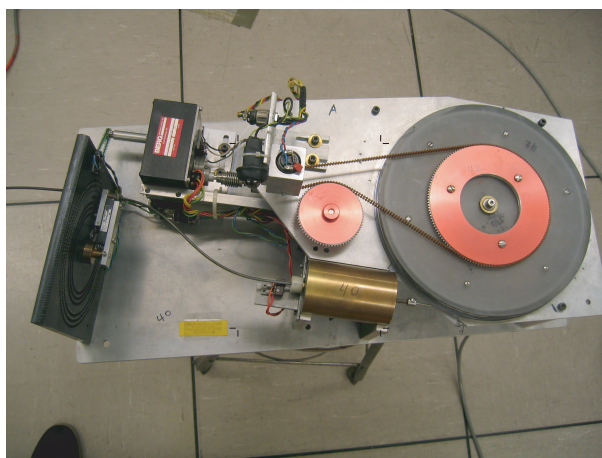


Figure 30: The storage reel for the source wire sits horizontally near the brass-clad storage pig where the active end of the wire is located. The indexer system is at the vertically-oriented black square plate. Two nylon source tubes are connected to the indexer on the left.

protect against wire-buckling during extension, there is a short stiff 0.035" OD wire (upper support wire) attached near the exit groove, in the region of the exit groove and a few cm into the storage groove. Recently, to prevent buckling when the wire is nearly fully extended and pushed with near-maximum force, it has been found helpful to have also a stiff lower support wire, 0.032" OD and nearly full-circle, between the spring fingers and the source wire.

Within the calorimeters, the source tubes are 15 gauge stainless steel hypodermic tubing, 1.32 mm OD and 0.97 mm ID. These tubes are coupled via 3.12 mm OD 1.85 mm ID acetal plastic tubing between the calorimeters and the source drivers. Various coupling schemes include commercial quick-release fittings for plastic tubing, or, at the indexers, small paraxial screws whose threads break into the tube sockets and bite into the plastic tubing. Transitions from plastic to metal typically involve small-angle conical holes in brass, leading to throats which shadow the ID of the stainless steel source tubes.

The reel position, which is generally a proxy for the position of the tip of the source wire, is given by an optical rotary encoder working in reversible quadrature mode (two square waves 90-degree out of phase). This can be read out, for example, by industrial batch counters which give local visual display. The batch counter can be read out via a standard PC com port. The indexer position is also quadrature encoded, one count per revolution, using micro-switches actuated by a cam on the Geneva drive which advances the index nozzle one tube per revolution, and read out similarly. Electrical control of the drivers has been via a circuit using magnetic reed relays, with local switch control of functions which can also be set to remote control via a TTL logic expansion card in a PC. The PC can digitize the DC currents of up to 48 photomultiplier tubes, using a high-sensitivity Operational Amplifier multichannel circuit with current to voltage conversion using resistors in the range of 1 to 20 Megaohms, feeding into an expansion card multichannel DVM reading at up to 150 Hz. Typical wire speeds are between 5 and 15 cm/s, but it is possible to run the wire somewhat slower if desired during data taking. Alternatively, the source driver control and the DC current data acquisition can be handled by different computers, with the source controller posting the reel and indexer positions and the source driver status for inclusion in the recorded data stream. A more recent compact version of the electrical control, position readouts, and network communication functionality is available using a logic state-engine circuit.

5.2 Laser and LED Systems

The conceptual layout of the HF light monitoring system is shown in Figure 31 and consists of three levels of light propagation and splitters.

1. 1 → 4 (level-1) UV laser light splitter,
2. 1 → 9 (level-2) Calibration Box (CBOX) laser and LED light splitter, and
3. 1 → 24 (level-3) Calibration Light Injector (CLI) into PMTs.

The laser calibration system uses a pulsed nitrogen laser with 300 μJ of nominal output power. It produces UV light pulses ($\lambda = 337$ nm) of a few nanoseconds length with a frequency of (10-20) Hz. The laser light is guided to the experimental hall by a 65 m long 300 μm diameter fused-silica fiber, connected to a 1 → 4 splitter. This division allows to serve the 4 quadrants of either HF+ or HF-. The splitter consists of a 800 μm diameter fused-silica core fiber with fluorine-doped fused-silica cladding which homogenizes and splits the light into four other fibers.

Each output fiber from the 1 → 4 splitter enters into a CBOX about 10 m downstream placed in one of the front-end electronics racks. The CBOX has 9 outputs (*i.e.* 1 → 9 splitter) to provide light to 9 RBXs of each HF quadrant. There are thus eight CBOXs in total for the two HF halves. Inside the CBOX, the UV laser light is converted into blue light by a blue-emitting plastic scintillator (Kuraray SCSN81). The input light intensity is monitored by PIN1 (see Figure 31). The plastic scintillator is attached to one end of a mixer, which is made of a polystyrene fine-polished parallelepiped. Two blue LEDs are also attached to this mixer adjacent to the scintillator as the alternative light source, which can be pulsed at high rates. The LEDs are pulsed by a custom-made module. The opposite end of the mixer is used to mount an 11-fiber bundle and a second PIN-diode (PIN2). Two of the 11 output fibers are read out by a third PIN-diode (PIN3) for the purpose of sampling the light intensity. The three PIN-diodes (Hamamatsu S6786) monitor light intensities at different levels to provide full coverage of dynamic range; they are digitized and read out using the same QIE front-end.

Light output from CBOX is transported to an RBX with a fiber. Each RBX houses a Calibration Light Injector (CLI) which transforms the calibration light into a uniform beam of light using a lens. This beam propagates through an air-core light guide, which holds a 120-fiber calibration bundle at its other end. The inner wall of the light guide is black-anodized to minimize reflections. The 120 fibers in the calibration bundle are distributed among the 24 PMTs, with 5 fibers per PMT.

5.2.1 Dynamic Range and Single Photoelectron Calibration

The calibration system is designed to allow measurement of input light intensity over four orders of magnitude using PIN-diodes. For any light intensity, at least one of the three PIN-diodes is always capable of providing a measurement. Full laser intensity saturates the QIE channel, digitizing the PMT signal. Therefore, attenuation factors of $10^4 - 10^5$ are typically applied in order to perform single photoelectron (1 p.e.) calibration; see Figure 32. The LED subsystem is less intense, and saturation level is generally not reached.

The PMTs are subdivided into three gain groups: low, medium, and high gain. Figure 32 represents a PMT from the medium gain group. The separation of the single p.e. depends on the PMT gain or high voltage and the single p.e. peak becomes well-defined for voltages higher than -1250 V for most of the PMTs. The dependence of the PMT gain on applied high voltage is demonstrated in Figure 33. Generally, a 100 V change in high voltage gives a factor of 1.5 in PMT gain. Using well-resolved single photoelectron peaks, the calibration error is about 3%. However, for the low gain PMTs, we estimate this calibration error to be up to 10% at $HV = -1250$ V and up to 20% at $HV = -1150$ V. At $HV = -1250$ V, the PMT gains (in terms of single photoelectron calibration) range from 6 to 20 QIE counts per photoelectron.

The output signal uniformity of the nine channels of CBOX was measured using a single PMT and was found to be 3-4%. Several CBOXs were also measured in the lab and 5% spread was observed.

The distribution of PMT responses to fixed laser light intensity, Figure 34, characterizes the uniformity of the overall light calibration system. The histogram includes measurements from 144 PMTs contained

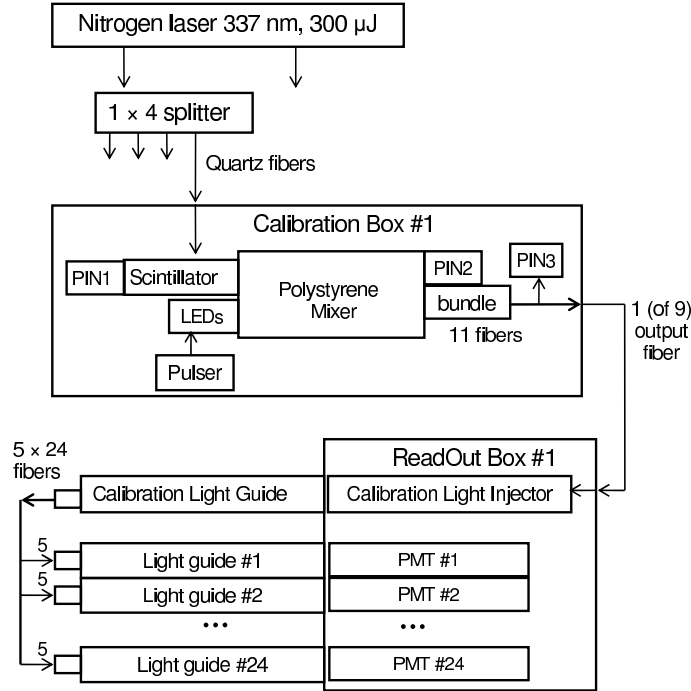


Figure 31: Conceptual layout of the light calibration system for the HF calorimeters.

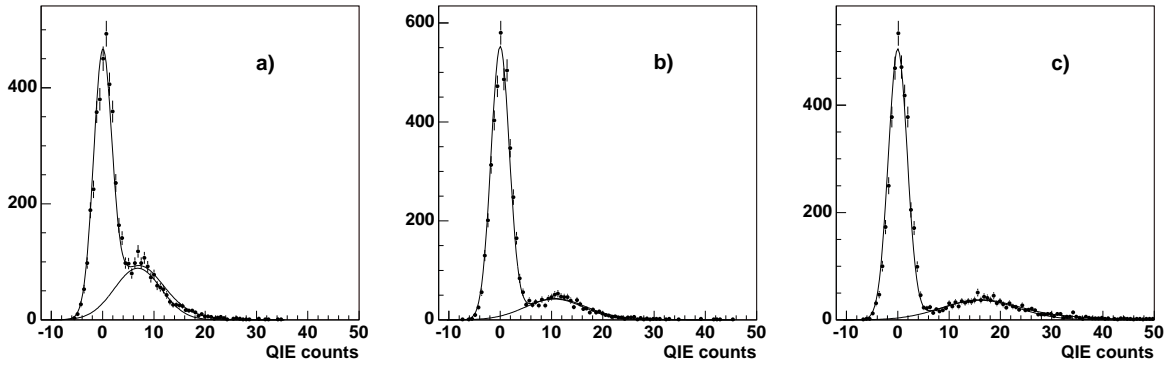


Figure 32: The amplitude spectra (pedestal subtracted) of a PMT exposed to low intensity laser light and operated at different high voltage: a) -1150 V, b) -1250 V, c) -1350 V. The spectra are fitted to the sum of two Gaussians. The peak at zero represents the pedestal signal; the second peak is due to single photoelectrons.

in six RBXs. Note that the data collected from different wedges (two RBXs calibrated at once) are normalized to the same input light using the PIN-diodes measurements.

The RMS of the distribution is about 15%, significantly higher than the (3-5)% spread of CBOX output signals. This is understood in terms of additional non-uniformity introduced by the level-3 splitter injecting light into PMTs. The 7% CLI non-uniformity, which makes up a good part of the overall non-uniformity of 15%, is consistent with the lab measurements performed when they were assembled, tuned, and tested. The CLIs were tested on an optical bench using a blue LED light source. The profile of the outgoing light spot at about 40 cm downstream (the location of the calibration fiber bundle) was measured with a 2 mm-diameter photo-diode, which yielded a non-uniformity of 8%. The 1% difference may be attributed to averaging over five calibration fibers, distributed randomly in the bundle, per PMT.

Another source of non-uniformity is the $1 \rightarrow 4$ splitter. Lab measurements show that it contributes up to 8% to the total spread. An estimate of total spread can be obtained by adding the non-uniformity of

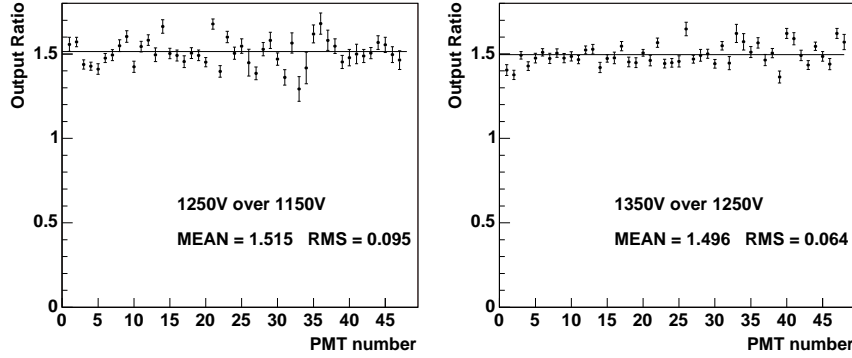


Figure 33: The ratios of single photoelectron responses at different high voltages. The figures show measurements of 48 PMTs corresponding to two RBXs.

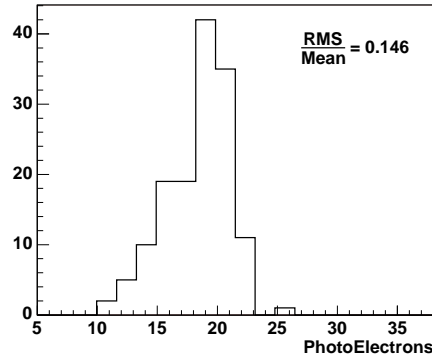


Figure 34: The distribution of 144 PMT responses, in units of photoelectrons, to the same intensity calibration laser light.

the three levels of light splitters, which leads to a value of 17% for the total spread.

5.2.2 Saturation of Readout Channels

Saturation of the readout channel takes place because of the limited dynamic range of the QIEs. The measurements of saturation levels, in units of photoelectrons, are displayed in Figure 35. Saturation is revealed as a deviation from the flat behavior of the relative (to input light intensity) PMT response as a function of the input light intensity.

The saturation level for each PMT readout channel can then be converted, using beam data, from units of photoelectrons into units of energy of incident particle in order to infer the HF dynamic range. We constructed three saturation plots for -1150 V, -1250 V, and -1350 V, based on electron and pion beam data. The plots were analyzed in conjunction with the single p.e. resolving ability at these high voltages (see Figure 32). The optimal gain (high voltage) is found by setting separately the appropriate HV for each of the three PMT gain group. This results in the following HV distribution in terms of the towers in the HF wedge: -1150 V for the outer, -1250 V for the middle, and -1350 V for the inner PMTs.

For a simplified “intermediate optimum” we can set $HV = -1250$ V for all the PMT channels. If we use the 100 GeV electron beam data for conversion, more than half of the L channels saturate in the energy range of 2-3 TeV and the S channels at energies above 6 TeV.

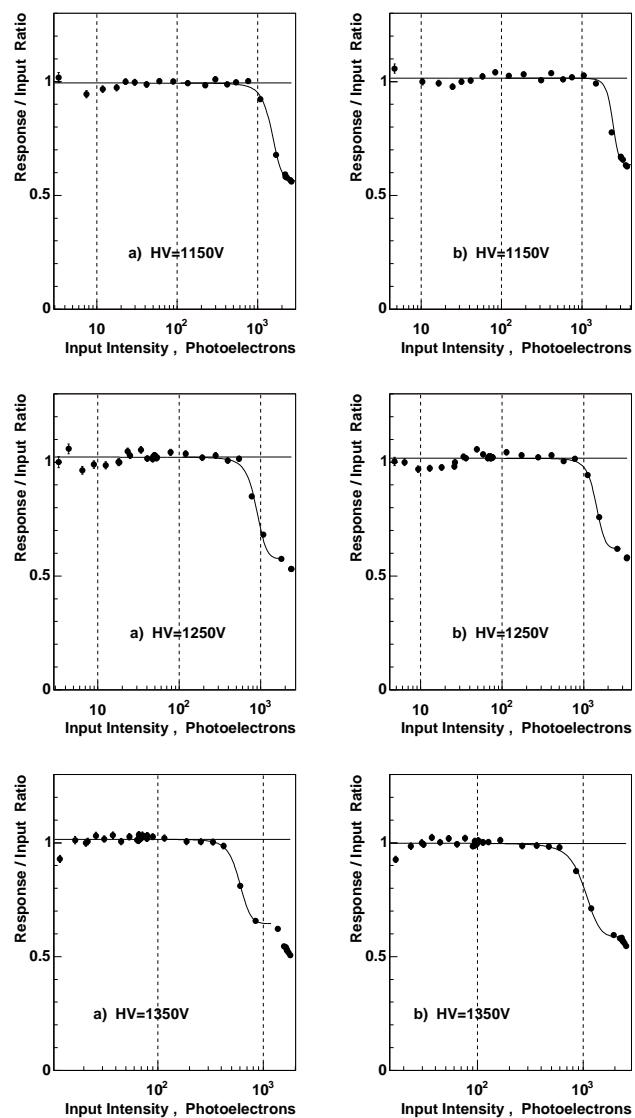


Figure 35: Dependence of the PMT response on the input laser light intensity for a) a high gain PMT, b) a low gain PMT, at different applied high voltages clearly show the saturation level as deviation from linearity.

5.3 Radiation Monitoring Systems

5.3.1 Neutrons, Charged Particles and Gammas Around HF

The HF radiation monitoring system includes neutron counters MNR-14 (8 per each HF) to measure the neutron fluence, and dosimeters KG-18 (2) and KG-21 (2) to measure the total ionization dose due to the γ and charged particles. The KG-21 counters are placed inside the shielding between absorber and PMTs. The KG-18 counters and neutron monitors are positioned in the vicinity of the readout boxes and the electronics racks. The relevant parameters for the radiation monitors are shown in the Table 6.

Table 6: The detectors used for radiation monitoring in the HF area.

Detector	Location	Number	Detected radiation	Dynamic range	Expected count rate (pulses/s)
MNR-14	RBXs / racks	16	neutrons	up to 5×10^6 n/cm ² /s	$10 - 10^4$
KG-21	fiber / PMTs	4	charged/ γ	$1 - 10^4$ R/hour	0.1-100
KG-18	RBXs / racks	4	charged/ γ	$6 \times 10^2 - 3 \times 10^4$ R/hour	0.01-10

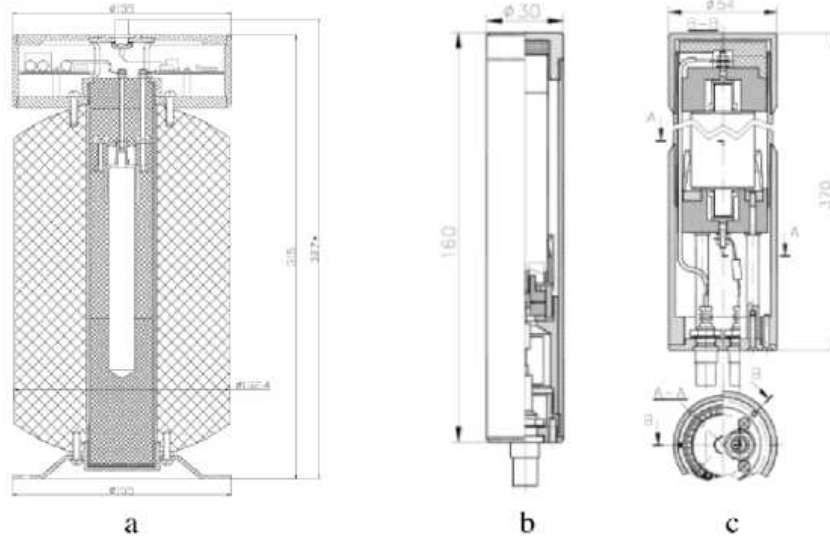


Figure 36: The details of the neutron monitor MNR-14 (a), KG-18 (b) and KG-21 (c) dosimeters are schematically shown above.

The drawings of the detectors are shown in Figure 36. All monitors are designed to operate autonomously for long periods of time. Neutron detection is based on $^{10}\text{B}(n, \alpha)^7\text{Li}$ reaction induced by the slow neutrons in the argon-filled proportional counter surrounded by a 6-inch-diameter polyethylene moderator (see Figure 36.a). The electronics enclosure includes a Cockroft-Walton voltage multiplier and a signal conditioning unit. KG-18 (Figure 36.b) and KG-21 (Figure 36.c) are low noise ionization chambers with aluminum shells. These counters use an external high voltage power supply. Each detector is connected to the readout electronics with a single cable (for both signal and power supply).

The readout electronics includes ADCs and scalars. The whole system is controlled by DIM server running under Windows OS. The total data rate is expected to be at the level of 100 bytes/s.

The elements of the system have been tested and calibrated with the radioactive source. The additional beam tests of the neutron monitors have shown a good agreement of the measured neutron rates with Monte Carlo calculations.

5.3.2 Monitoring of Fibers

A system based on the optical reflectometry concept has been developed and installed in selected detector locations to monitor the optical degradation due to radiation and recovery of the fibers. The dynamic nature of damage and recovery processes demand rapid assessment of optical transparency, especially at the wavelength region where the PMTs are the most sensitive.

We use a pulsed nitrogen laser (337 nm) and it is wavelength shifted into the blue region (~ 440 nm) by a 2 cm long scintillating fiber positioned in a feed-through connector. This light is then distributed into fibers in four wedges per HF. Within a wedge, 7 towers (spanning all rapidity regions) are instrumented with these sample fibers. Each fiber is readout by the PMT that serves that particular tower. In total, there are 56 sample fibers in the entire system which will provide radiation damage information. The optical light distribution is designed such that the first reflection occurs at an optical connector before the light is injected into the sample fiber (see Figure 37.a). This pulse provides a reference point. The injected light gets reflected from the fiber end and detected by the PMT 25 ns later. The charge ratio of the reflected pulse from the fiber tip to the pulse from the first optical connector is used as a measure of fiber darkening.

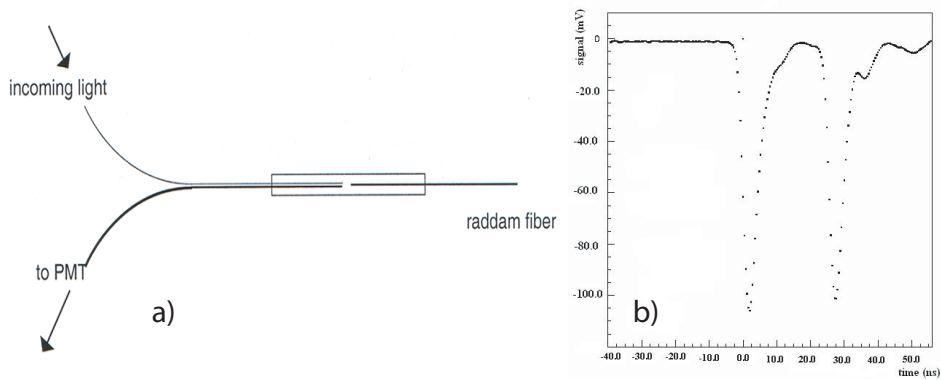


Figure 37: The radiation damage to the optical transparency is monitored by a set of 56 fibers distributed in the entire calorimeter system. The ratio of the reflected pulse from the far end of the fiber located inside the absorber to the reflected pulse from the first optical connector provides a relative measure of fiber darkening. A schematic of optical connection is depicted in (a) and a pulse train is reproduced in (b).

6 Monte Carlo Simulations and Parameterization

6.1 GEANT4 Simulation

The GEANT4 [15] toolkit is used to simulate a full-size realistic HF calorimeter wedge as tested in the beam. The beam spot on the calorimeter is taken to be a $4 \times 4 \text{ cm}^2$ area with uniform particle distribution. The 600-micron diameter core quartz fibers with refractive index of 1.459 are clad with a plastic material with a refractive index of 1.409. Cherenkov photon generation is performed separately by using a simple algorithm. In this algorithm, when a charged particle above the Cherenkov threshold enters the fiber core, the number of photons for each GEANT4 step x is calculated by

$$N_\gamma = \left[2\pi\alpha \left(\frac{1}{\lambda_1} - \frac{1}{\lambda_2} \right) \sin^2 \theta_C \right] x. \quad (10)$$

The fine structure constant is represented by α , and θ_c is the Cherenkov angle. The wavelength range is taken from $\lambda_1 = 280 \text{ nm}$ to $\lambda_2 = 700 \text{ nm}$. The photon direction is randomized on a cone with an opening angle of $\theta = \cos^{-1}(1/\beta n_c)$ around the particle direction.

The photons whose direction fall within the numerical aperture (NA= 0.33) are traced through the fiber with attenuation ($\lambda \approx 15 \text{ m}$). Typical fiber length is 2.5 m. Photons emerging at the end of the fiber bundles are transported to PMTs through 40-cm long air-core reflective light guides. They are then converted to photoelectrons at the PMT photocathode with a peak quantum efficiency of 25% at 425 nm. The first dynode gain is taken to be 4.2, and Poisson statistics is also applied at this stage. We also added Gaussian noise ($\sigma = 0.5 \text{ GeV}$) to account for the front-end electronics noise.

We used two physics lists (LEHP-3.6 and QGSP-2.7) that are available within GEANT4. LHEP uses parametrized models for inelastic scattering whereas QGSP is a theory-driven modeling for energetic pion, kaon, and nucleon reactions. It employs the quark-gluon string and pre-equilibrium decay models with an extensive evaporation phase to model the nucleus behavior. QGSP-2.7 and FTFP-2.8 physics lists gave similar results as the QGSP-2.7.

6.2 Parametrized Simulation (HFast)

In addition to GEANT4, we developed a fast parametrization (HFast). There were three requirements: first, the parametrization must be faithful to all existing HF beam data as much as possible (no worse than 10%); second, it must be much faster ($\sim \text{ms/event}$) than GEANT4; and, third, the jet response should be calculable.

We use beam measurements to develop this parameterization. This is realized in the form of a *response generator*, which, given an impacting particle with a given energy, extracts a signal representing the response of the detector from a suitable distribution based on data. We use all the available beam response distributions. In cases where we do not have them, GEANT4 is used but always *normalized* to the real data.

The parametrization is split into two stages: *physics* and *electronics*. The *physics* stage takes the particle type and energy as input, and outputs a number of photoelectrons, which comes from the interaction of the original particle with the detector material, the capture of Cherenkov photons in the quartz fibers and their propagation through the fibers and light guides, and their conversion into photoelectrons in the photocathode of the PMT. These processes are not described in detail by this parametrization, but are condensed in a response distribution that represents the final number of photoelectrons and depends only on the particle type and energy.

The *electronics* stage of the parametrization takes the number of photoelectrons and produces a final signal that represents the electronic pulse resulting from multiplication of the photoelectrons in the PMT and electronics readout, including noise and calibration. This part is obviously independent of the incoming particle and energy.

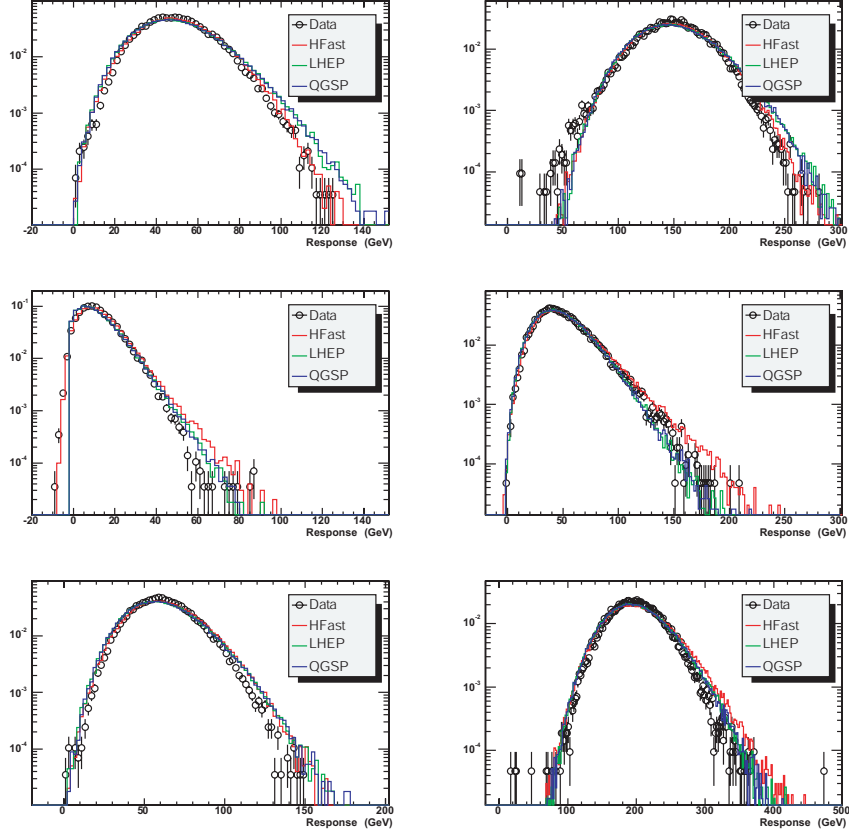


Figure 38: 50 (left) and 150 (right) GeV electron data are compared to two GEANT4 physics lists (LHEP and QGSP) and HFast. The experimental data are the same as in Figure 7, and the top row is L , the middle is S , and the bottom is $L + S$.

6.2.1 Physics Stage

For each impacting particle of energy E , a number of photoelectrons from the L fiber section is produced and extracted from a Poisson distribution with average λ :

$$P(k) = \sum_k \frac{\lambda^k}{k!} e^{-\lambda} \quad (11)$$

with the exception of muons. The average λ is in turn extracted from a Gaussian which includes additional resolution terms.

$$G(\lambda) = \frac{1}{\sqrt{2\pi}\sigma_\lambda} \exp\left(-\frac{(\lambda - \lambda_0)^2}{2\sigma_\lambda^2}\right) \quad (12)$$

$$\lambda_0 = p\alpha(E)E \quad (13)$$

$$\sigma_\lambda^2 = s_C^2 \lambda_0^2 + s_2^2 \lambda_0 \quad (14)$$

The meaning and values of the terms in the above formulae are shown in Table 7. Here, $\alpha(E)$ is a function that represents the relative response for different particles and is constant for electrons and photons. This is extracted from the full GEANT4 simulation and is shown for a number of particles in Figure 40.

The number of S photoelectrons is also extracted from a suitable distribution, and there is a correlation between the L and S responses for each event. We extract the correlation from GEANT4, as shown in Figure 41. For each event, after we extract the number of L photoelectrons from the distribution defined previously, we obtain the number of S photoelectron from a distribution function whose mean is a function of the number of L photoelectron, so that the two numbers will be correlated as in Figure 41.

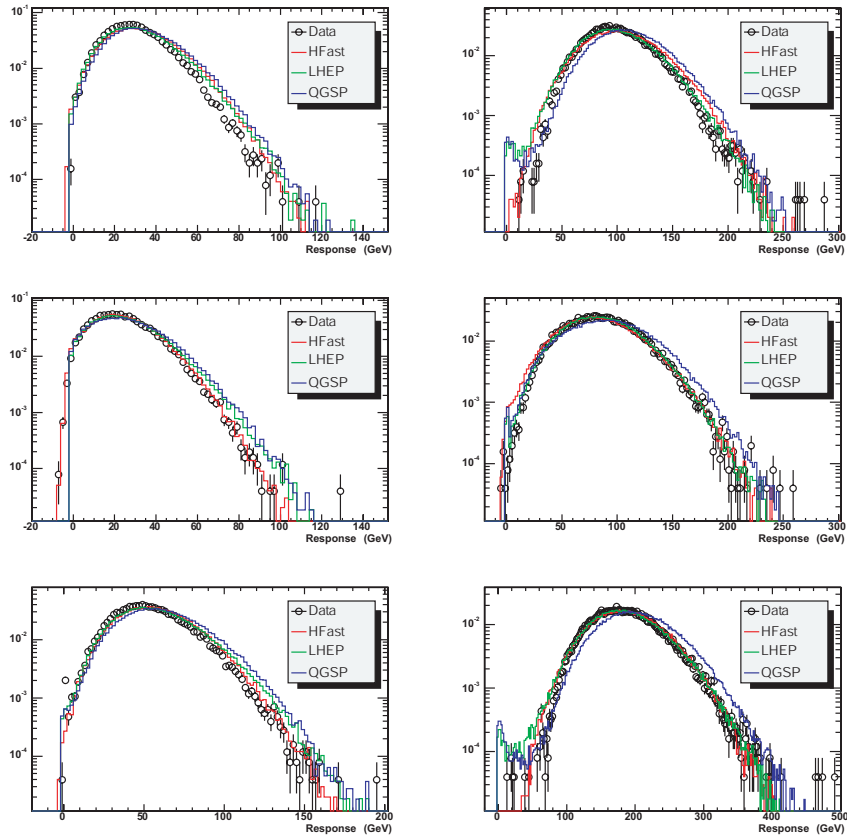


Figure 39: 50 (left) and 150 (right) GeV pion data are compared to two GEANT4 physics lists (LHEP and QGSP) and HFast. The experimental data are the same as in Figure 10, and the top row is L , the middle is S , and the bottom is $L + S$.

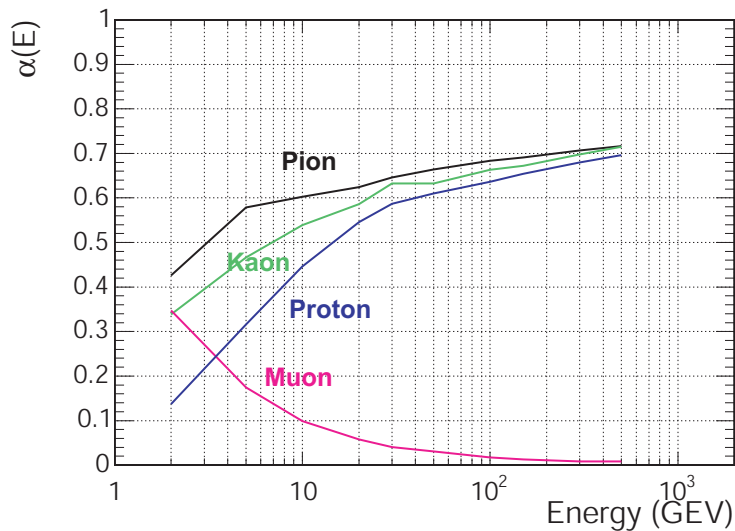


Figure 40: Relative responses of different types of particles are normalized to that of electrons as a function of energy, *i.e.* ‘particle/ e .’

The distribution of S electrons is also a convolution of a Gaussian and a Poisson distributions as described above, but only for hadrons. Electrons and photons lose a large fraction of their energy in the front part where there are no S fibers and are described by a slightly modified distribution.

Table 7: Meaning and the parameter values for the HFast physics stage are summarized below.

Parameter	Meaning	Electrons	Hadrons
p	p.e. per GeV	0.22/GeV	
$\alpha(E)$	$\pi/e,p/e, \dots$ ratio	1	see Figure 40
s_c	constant term	10%	11%
s_2	hadron term	0	0.6

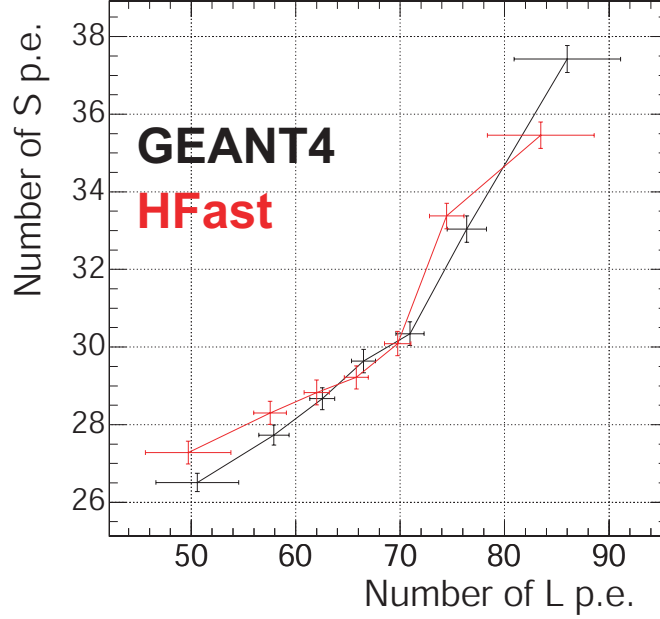


Figure 41: Correlation between the number of L and S photoelectrons for 300 GeV electrons from GEANT4 simulation *vs* the HFast parametrization.

6.2.2 Electronics Stage

After a number of photoelectrons is produced from an interaction, any relation with the impacting particle type and energy is lost. The photo-multiplication and read-out is then only dependent on the number of photoelectrons and on the channel type (L or S) through a calibration factor, which is tuned to 100 GeV electron data. For each photoelectron, a response from the detector is produced as a Gaussian distributed signal with a mean of μ (calibration factor) and deviation $\sigma = 0.3\mu$ (tuned to data):

$$G(x) = \frac{1}{\sqrt{2\pi}\sigma} \exp\left(-\frac{(x - \mu)^2}{2\sigma^2}\right) \quad (15)$$

A Gaussian noise term is added which depends on the high voltage. We extracted from data that, at the nominal PMT gain,

$$L \approx 0.6\sqrt{N_t} \text{ GeV}, \quad (16)$$

$$S \approx 0.85\sqrt{N_t} \text{ GeV} \quad (17)$$

where N_t is the number of towers used.

6.2.3 Jet Energy Response and Resolution

Using a sample of jets simulated by PYTHIA ($W \rightarrow jj$), we estimated the jet energy resolution and the combination of L and S components that makes the response the most linear. The original jet energy

E_{JET} is defined as the sum of the energy of all particles in the jet, and the intrinsic energy resolution is the difference between the original jet energy and the energy measured by the HF, E_{DET} , divided by the energy detected, assuming that the jet is fully contained in HF. E_{DET} is obtained from the parametrization described above.

The jet energy resolution is shown in Figure 42.a with black circles ($\theta = 0$) and ranges from 65% at 35 GeV to a plateau of 25%, starting at about 500 GeV. Here, the detected energy comes from L fibers only, and is non-linear with jet energy. A combination of L and S signals is more suitable for restoring linearity in the jet energy scale. Assuming that the typical jet composition is well represented by PYTHIA, we search for the best combination of L and S signals that results in response linearity. We parametrize this with an angle θ :

$$E_{\text{DET}} = C(\theta) [L \cos(\theta) + S \sin(\theta)] \quad (18)$$

and search for a value of α that gives a constant relative response $(E_{\text{JET}} - E_{\text{DET}})/E_{\text{JET}}$. As shown in Figure 42.b for a number of α values, this takes place for $\theta = 4\pi/5$. The energy resolution clearly degrades (from 65% at 35 GeV to about 34% at 1 TeV) in order to achieve a linear response.

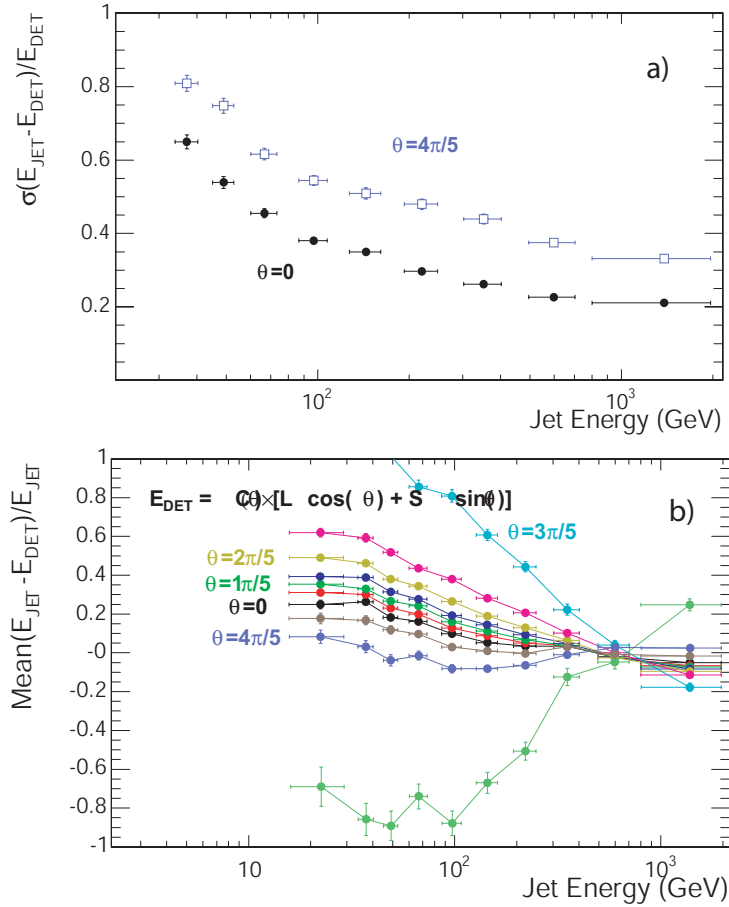


Figure 42: Jet energy resolution of HF, as a function of energy, with the optimal combination of the L and S signals is shown by open squares ($\theta = 4\pi/5$) in (a), and the calculated jet responses are shown in (b) for a variety of θ values.

HFast reproduces test beam data with 10% accuracy and is reliable at predicting the detector response to all types of different particles. The parametrization output provides signals for both L and S sections, including correlation between them, electronics noise, and the calibration.

Figure 43 contrasts the electromagnetic and hadronic energy resolutions calculated by all the simulations methods described here. The data points are also included.

Table 8: The measured and simulated electromagnetic energy resolutions using high energy electrons for L and the combined $L + S$ sections, quoted in percentage below, are in good agreement. The errors are statistical only. TB refers to experimental data. LHEP is one the parametrized physics lists in GEANT4. HFast refers to a separate parametrized simulation developed for the HF calorimeters (see text for details).

	30 GeV	50 GeV	100 GeV	150 GeV
TB (L)	39.5 ± 0.3	31.6 ± 0.2	23.4 ± 0.1	20.0 ± 0.1
TB ($L + S$)	37.2 ± 0.3	29.3 ± 0.2	21.5 ± 0.1	18.3 ± 0.1
LHEP (L)	44.7 ± 0.6	35.4 ± 0.4	25.3 ± 0.3	22.0 ± 0.2
LHEP ($L + S$)	40.6 ± 0.5	32.7 ± 0.4	23.7 ± 0.3	20.6 ± 0.2
HFast (L)	42.0 ± 0.5	33.0 ± 0.5	24.4 ± 0.5	20.6 ± 0.5
HFast ($L + S$)	40.3 ± 0.5	31.9 ± 0.5	24.2 ± 0.5	21.3 ± 0.5

Table 9: The measured and simulated hadronic energy resolutions using high energy pions for L and the combined $L + S$ sections, quoted in percentage below, are in good agreement. The errors are statistical only. TB refers to experimental data. LHEP and QGSP are two physics lists in GEANT4. HFast refers to a separate parametrized simulation developed for the HF calorimeters (see text for details).

	30 GeV	50 GeV	100 GeV	150 GeV
TB (L)	58.6 ± 0.4	45.2 ± 0.3	33.9 ± 0.2	27.9 ± 0.2
TB ($L + S$)	53.3 ± 0.4	40.1 ± 0.3	30.2 ± 0.2	25.6 ± 0.2
LHEP (L)	62.8 ± 0.9	48.3 ± 0.6	33.7 ± 0.4	28.7 ± 0.3
LHEP ($L + S$)	53.8 ± 0.7	40.4 ± 0.5	29.3 ± 0.3	25.3 ± 0.3
QGSP (L)	59.6 ± 0.8	46.8 ± 0.6	32.0 ± 0.4	26.9 ± 0.3
QGSP ($L + S$)	50.8 ± 0.7	40.2 ± 0.5	29.1 ± 0.3	24.9 ± 0.3
HFast (L)	58.8 ± 0.5	46.5 ± 0.5	34.8 ± 0.5	30.3 ± 0.5
HFast ($L + S$)	49.5 ± 0.5	38.9 ± 0.5	29.5 ± 0.5	26.2 ± 0.5

Table 10: The measured and simulated electromagnetic responses using electrons for L and the combined $L + S$ sections, are given in GeV below. The errors are statistical only. TB refers to experimental data. LHEP is one the parametrized physics lists in GEANT4. HFast refers to a separate parametrized simulation developed for the HF calorimeters.

	30 GeV	50 GeV	100 GeV	150 GeV
TB (L)	29.5 ± 0.1	49.6 ± 0.1	100.0 ± 0.0	149.1 ± 0.2
TB ($L + S$)	35.5 ± 0.1	61.6 ± 0.1	130.0 ± 0.0	199.5 ± 0.3
LHEP (L)	30.3 ± 0.2	50.1 ± 0.3	100.4 ± 0.4	150.1 ± 0.5
LHEP ($L + S$)	37.1 ± 0.2	64.1 ± 0.3	133.5 ± 0.5	206.3 ± 0.6
HFast (L)	29.9 ± 0.5	49.9 ± 0.5	99.9 ± 0.5	150.0 ± 0.5
HFast ($L + S$)	36.1 ± 0.5	62.7 ± 0.5	130.9 ± 0.5	202.4 ± 0.6

7 Conclusions

The understanding of special features of fused-silica fiber based calorimeters has matured in recent years. Much information has come from prototypes, radiation exposures, and the HF wedge beam tests. CMS forward calorimeters are designed to identify high energy jets with adequate precision, *e.g.* 20 to 30

We have shown that 5% calibration using radioactive source signals is achievable. The monitoring systems based on LED and laser pulses have been successfully used and expected to be effective monitoring tools during the operation of these detectors.

Table 11: The measured and simulated hadronic energy responses using pions for L and the combined $L + S$ sections are quoted in GeV. The errors are statistical only. TB refers to experimental data. LHEP and QGSP are two of physics lists in GEANT4. HFAST refers to a separate parametrized simulation developed for the HF calorimeters.

	30 GeV	50 GeV	100 GeV	150 GeV
TB (L)	18.4 ± 0.1	32.7 ± 0.1	70.2 ± 0.2	108.8 ± 0.3
TB ($L + S$)	31.5 ± 0.1	57.7 ± 0.2	126.7 ± 0.3	197.9 ± 0.3
LHEP (L)	19.3 ± 0.2	33.8 ± 0.2	70.3 ± 0.4	108.1 ± 0.5
LHEP ($L + S$)	33.9 ± 0.3	61.7 ± 0.4	132.1 ± 0.6	202.9 ± 0.8
QGSP (L)	20.9 ± 0.2	36.4 ± 0.3	76.2 ± 0.4	116.8 ± 0.5
QGSP ($L + S$)	37.1 ± 0.3	65.2 ± 0.4	140.3 ± 0.6	216.9 ± 0.8
HFAST (L)	19.6 ± 0.5	33.2 ± 0.5	68.1 ± 0.5	103.9 ± 0.5
HFAST ($L + S$)	32.8 ± 0.5	57.7 ± 0.5	122.6 ± 0.5	187.4 ± 0.5

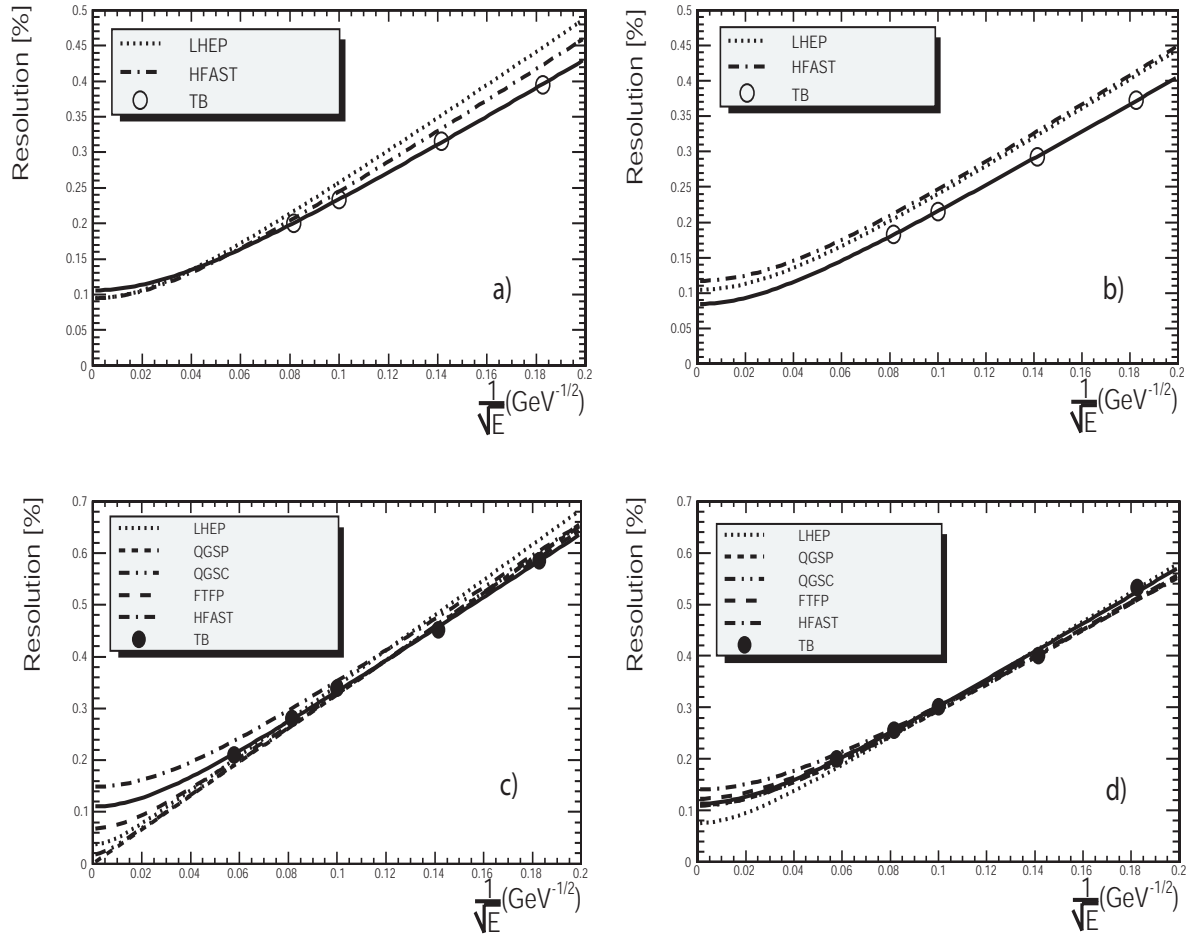


Figure 43: The electromagnetic for (a) L , and (b) $L + S$; and the hadronic (c) L , and (d) $L + S$ energy resolutions are compared for several simulations studied here. The beam data are indicated by markers (TB) in each case and the fitted curves to data are shown in solid lines.

8 Acknowledgments

This project was carried out with financial support from CERN, the U.S. Department of Energy, RMKI-KFKI (Hungary, OTKA grant T 016823), the Scientific and Technical Research Council of Turkey (TÜBİTAK), Turkish Atomic Energy Agency (TAEK), Bogazici University Research Fund (Grant no:

04B301), the Russian Ministry for Education and Science and the Russian State Committee for Atomic Energy.

References

- [1] The CMS Collaboration. Technical Proposal. CERN/LHCC 94-39, 1994.
- [2] The CMS Collaboration, *The Hadron Calorimeter Project Technical Design Report*, CERN/LHCC 97-31 (1997).
- [3] N. Kauer *et al*, Physics Letters **B** 503 (2001) 113-120.
- [4] N. Akchurin *et al*, CMS Note 2002/016.
- [5] N. Akchurin *et al*, Nucl. Instr. and Meth. A379 (1996) 526-527.
- [6] N. Akchurin *et al*, Nucl. Instr. and Meth. A399 (1997) 202-226.
- [7] N. Akchurin *et al*, Nucl. Instr. and Meth. A400 (1997) 267-278.
- [8] N. Akchurin *et al*, Nucl. Instr. and Meth. A408 (1998) 380-396.
- [9] N. Akchurin *et al*, Nucl. Instr. and Meth. A409 (1998) 593-597.
- [10] A. S. Ayan *et al*, J. Phys. G: Nucl. Part. Phys. **30** (2004) N33-N44.
- [11] N. Akchurin and R. Wigmans, Review of Scientific Instruments, Vol 74, No 6 (2002).
- [12] I. Dumanoglu *et al*, Nucl. Instr. and Meth. A490 (2002) 444-455.
- [13] N. Akchurin *et al*, Nucl. Instr. and Meth. B187 (2002) 66-78.
- [14] R. Thomas, MS Thesis, Texas Tech University, (2004).
- [15] S. Agostinelli *et al*, Nucl. Inst. Meth. A **506** (2003) 250-303. We use GEANT4 version 4.7.0.p01.